The *XMM* Cluster Survey analysis of the *SDSS* DR8 redMaPPer catalogue: implications for scatter, selection bias, and isotropy in cluster scaling relations

P. A. Giles [1]★ A. K. Romer [1]★ R. Wilkinson [1] A. Bermeo,[1] D. J. Turner [1]★ M. Hilton [2,3]
E. W. Upsdell [1] P. J. Rooney,[1] S. Bhargava,[1,4] L. Ebrahimpour [5,6] A. Farahi [7] R. G. Mann [8]
M. Manolopoulou,[8] J. Mayers,[1] C. Vergara,[1] P. T. P. Viana [5,6] C. A. Collins,[9] D. Hollowood [10]
T. Jeltema [10] C. J. Miller [11] R. C. Nichol,[12] R. Noorali,[10] M. Splettstoesser[10] and J. P. Stott[13]

[1]*Department of Physics and Astronomy, University of Sussex, Brighton BN1 9QH, UK*
[2]*Astrophysics Research Centre, University of KwaZulu-Natal, Westville Campus, Durban 4041, South Africa*
[3]*School of Mathematics, Statistics, and Computer Science, University of KwaZulu-Natal, Westville Campus, Durban 4041, South Africa*
[4]*AIM, CEA, CNRS, Université Paris-Saclay, Université Paris Diderot, Sorbonne Paris Cité, F-91191 Gif-sur-Yvette, France*
[5]*Instituto de Astrofísica e Ciências do Espaço, Universidade do Porto, CAUP, Rua das Estrelas, P-4150-762 Porto, Portugal*
[6]*Departamento de Física e Astronomia, Faculdade de Ciências, Universidade do Porto, Rua do Campo Alegre, 687, P-4169-007 Porto, Portugal*
[7]*Department of Statistics and Data Sciences, The University of Texas at Austin, Austin, TX 78712, USA*
[8]*Institute for Astronomy, University of Edinburgh, Royal Observatory, Blackford Hill, Edinburgh EH9 3HJ, UK*
[9]*Astrophysics Research Institute, Liverpool John Moores University, Liverpool Science Park, 146 Brownlow Hill, Liverpool L3 5RF, UK*
[10]*Santa Cruz Institute for Particle Physics, University of California, Santa Cruz, 1156 High St, Santa Cruz, CA 95064, USA*
[11]*Department of Astronomy, University of Michigan, Ann Arbor, MI 48109, USA*
[12]*Institute of Cosmology and Gravitation, Dennis Sciama Building, Burnaby Road, Portsmouth PO1 3FX, UK*
[13]*Department of Physics, Lancaster University, Lancaster LA1 4YB, UK*

ABSTRACT

In this paper, we present the X-ray analysis of *Sloan Digital Sky Survey* DR8 redMaPPer (SDSSRM) clusters using data products from the *XMM* Cluster Survey (XCS). In total, 1189 SDSSRM clusters fall within the *XMM–Newton* footprint. This has yielded 456 confirmed detections accompanied by X-ray luminosity (L_X) measurements. Of these clusters, 381 have an associated X-ray temperature measurement (T_X). This represents one of the largest samples of coherently derived cluster T_X values to date. Our analysis of the X-ray observable to richness scaling relations has demonstrated that scatter in the T_X–λ relation is roughly a third of that in the L_X–λ relation, and that the L_X–λ scatter is intrinsic, i.e. will not be significantly reduced with larger sample sizes. Analysis of the scaling relation between L_X and T_X has shown that the fits are sensitive to the selection method of the sample, i.e. whether the sample is made up of clusters detected 'serendipitously' compared to those deliberately targeted by *XMM*. These differences are also seen in the L_X–λ relation and, to a lesser extent, in the T_X–λ relation. Exclusion of the emission from the cluster core does not make a significant impact on the findings. A combination of selection biases is a likely, but yet unproven, reason for these differences. Finally, we have also used our data to probe recent claims of anisotropy in the L_X–T_X relation across the sky. We find no evidence of anistropy, but stress this may be masked in our analysis by the incomplete declination coverage of the *SDSS*.

Key words: galaxies: clusters: general – X-rays: galaxies: clusters – X-rays: general.

1 INTRODUCTION

Clusters of galaxies are the largest gravitationally bound objects in the Universe, residing at the intersections of the dark matter filamentary structure. Enabled by a new generation of imaging surveys, from across the electromagnetic spectrum, clusters are expected to play an important role in forthcoming attempts to measure cosmological parameters to percent level accuracy (e.g. see fig. G2 in The LSST Dark Energy Science Collaboration 2018). Several detection methods will be used to deliver cluster samples of sufficient size, quality, and redshift grasp to meet the requirements of Stage IV (and beyond) Dark Energy Experiments (Dodelson et al. 2016). These methods include detections of spectral distortions to the Cosmic Microwave Background (CMB), of extended X-ray emission, and of projected overdensities (in the optical/near-IR band) of member galaxies. Relevant, ongoing, or soon to begin, experi-

★ E-mail: p.a.giles@sussex.ac.uk (PAG); romer@sussex.ac.uk (AKR); david.turner@sussex.ac.uk (DJT)

ments include the South Pole Telescope, the Atacama Cosmology Telescope, the Simons Observatory (CMB)[1], the *eROSITA* telescope (X-ray)[2], the Dark Energy Survey (DES), the Hyper Suprime-Cam Subaru Strategic Program, the Legacy Survey of Space and Time, and the *EUCLID* mission (optical/near-IR)[3].

Even after these new cluster samples become available, there will remain significant challenges to overcome before unbiased cosmological parameters can be reliably extracted. This has been illustrated by the surprising inconsistency between parameter estimates derived from clusters compared to those derived, using different techniques, from the same input data. For example, there is a 2.4σ tension with the DES Y1 galaxy clustering and cosmic shear results (Abbott et al. 2019). Similar tension was found by the Planck team when comparing their analysis of clusters with the CMB anisotropy spectrum (Planck Collaboration XXIV 2016). One way to address those challenges is to exploit synergies between data sets collected at different wavelengths (e.g. Wu, Rozo & Wechsler 2010; Grandis et al. 2021). The work presented herein aims to provide X-ray support to the efforts of the DES and LSST-DESC[4] collaborations to realize the potential of optical/near-IR detected clusters for cosmological studies. For this, we use X-ray data collected by the *XMM–Newton* telescope and analysed by the *XMM* Cluster Survey team (Romer et al. 2001). We focus specifically on clusters identified using the red-sequence Matched-filter Probabilistic Percolation technique (or redMaPPer; Rykoff et al. 2014, 2016, hereafter RM). However, this work will also be analogous to other cluster samples generated from optical/near-IR surveys, e.g. those identified using the CAMIRA (Oguri 2014) or WaZP (Aguena et al. 2021) algorithms.

The extraction of cosmological parameters from RM samples relies on the use of a Mass Observable Relation (MOR), i.e. a description of how the dark matter halo mass scales with the detection observable. The latter is quantified in RM samples by the so-called *richness* measure, which describes the number of galaxies detected per cluster (see Section 2.1 for more information). The halo mass is estimated from the weak lensing (WL) signal. However, the signal per cluster is so small that it is necessary to bin the sample, by richness and redshift, in order to measure the MOR (McClintock et al. 2019). The main drawback of this binning, or 'stacking' method is the loss of any information about the intrinsic scatter of the observable with mass. As shown in Sahlén et al. (2009), knowledge of the scatter and, its evolution with mass and redshift, is needed for accurate parameter estimation. The benefit of X-ray follow-up, such as that described herein, is that an X-ray observable to richness scaling relation will provide information about the scatter in the stacked MOR (e.g. Farahi et al. 2019).

Another drawback of using WL to calibrate the MOR for RM samples, is that the WL signal is diluted if there is an offset between the RM determined cluster centroid and the dark matter halo centre of mass. The impact of the offset needs to be modelled to mitigate the impact on derived cosmological parameters, for which X-ray follow-up is essential. This is because the X-ray surface brightness is a much better tracer of the underlying mass than the projected galaxy density. This type of mis-centring correction using X-ray data has been demonstrated in e.g. McClintock et al. (2019).

In summary, the work presented herein was motivated by the desire to support RM cluster cosmology in two ways: estimating intrinsic scatter on the MOR and determining a mis-centering model. The first step required to meet both goals is to gather as much high quality X-ray data as possible, and in Section 2 we discuss the development of RM cluster samples with X-ray observations in the *XMM* public archive. The X-ray analysis of these clusters is described in Section 3. We go on to present scaling relations between X-ray and RM observables, and their associated scatter, in Section 4. Analysis of the samples for the purposes of mis-centering modelling is the subject of a companion publication (Zhang et al. 2019). In Section 5, we explore the impact of selection bias on scaling relation scatter measurements by splitting the sample into clusters detected serendipitously and those specifically targeted by *XMM*. We also investigate a recent claim of anisotropy in scaling relations across the sky. Conclusions are summarized in Section 6 throughout this paper we assume a cosmology of $\Omega_M = 0.3$, $\Omega_\Lambda = 0.7$, and $H_0 = 70$ km s^{-1} Mpc^{-1}.

2 DEVELOPMENT OF THE SDSSRM–XCS CLUSTER SAMPLES

In this section, we describe the construction of the X-ray cluster samples used throughout this work. The process starts with the parent *SDSS* optical cluster catalogue described in Rykoff et al. (2014). A flowchart outlining the various steps involved is shown in Fig. 1.

2.1 The *SDSS* redMaPPer cluster catalogue

The red-sequence Matched-filter Probabilistic Percolation (again, denoted RM throughout), cluster finding algorithm (Rykoff et al. 2014), is a powerful tool for finding clusters from optical/near-IR photometric survey data and has already been successfully applied to *SDSS* (Rykoff et al. 2014) and DES (Rykoff et al. 2016). RM self-trains the red-sequence model to any available spectroscopic redshifts, and then calculates, in an iterative fashion, photometric redshifts for each cluster identified. The richness estimated by RM (hereafter, λ_{RM}) of each cluster is calculated as the sum of membership probabilities over all galaxies within a scale radius, R_λ, where $R_\lambda = 1.0\,h^{-1}$ Mpc$(\lambda/100)^{0.2}$. The specific RM cluster sample used throughout this work is based upon the 8th data release of the *Sloan Digital Sky Survey*[5] (or SDSS-DR8; Aihara et al. 2011). The RM *SDSS*-DR8 catalogue (Rykoff et al. 2014) contains a total of 396 047 clusters. The analysis was restricted to clusters with $\lambda_{RM} > 20$, because numerical simulations show that, at this threshold, 99 per cent of RM clusters can be unambiguously mapped to an individual dark matter halo (Farahi et al. 2016). Based upon this λ_{RM} cut, our initial sample contained 66 028 clusters (we denote this as the 'SDSSRM' sample hereafter, see Table 1).

2.2 The XCS image data base and source catalogue

The results presented in this paper were derived using X-ray data from all publicly available *XMM* observations[6] (as of 2018 September) with usable European Photon Imaging Camera (EPIC) science data. The *XMM* observations were analysed as part of the *XMM* Cluster Survey (Romer et al. 2001, hereafter XCS). The aim of XCS is to catalogue and analyse all X-ray clusters detected during the *XMM*
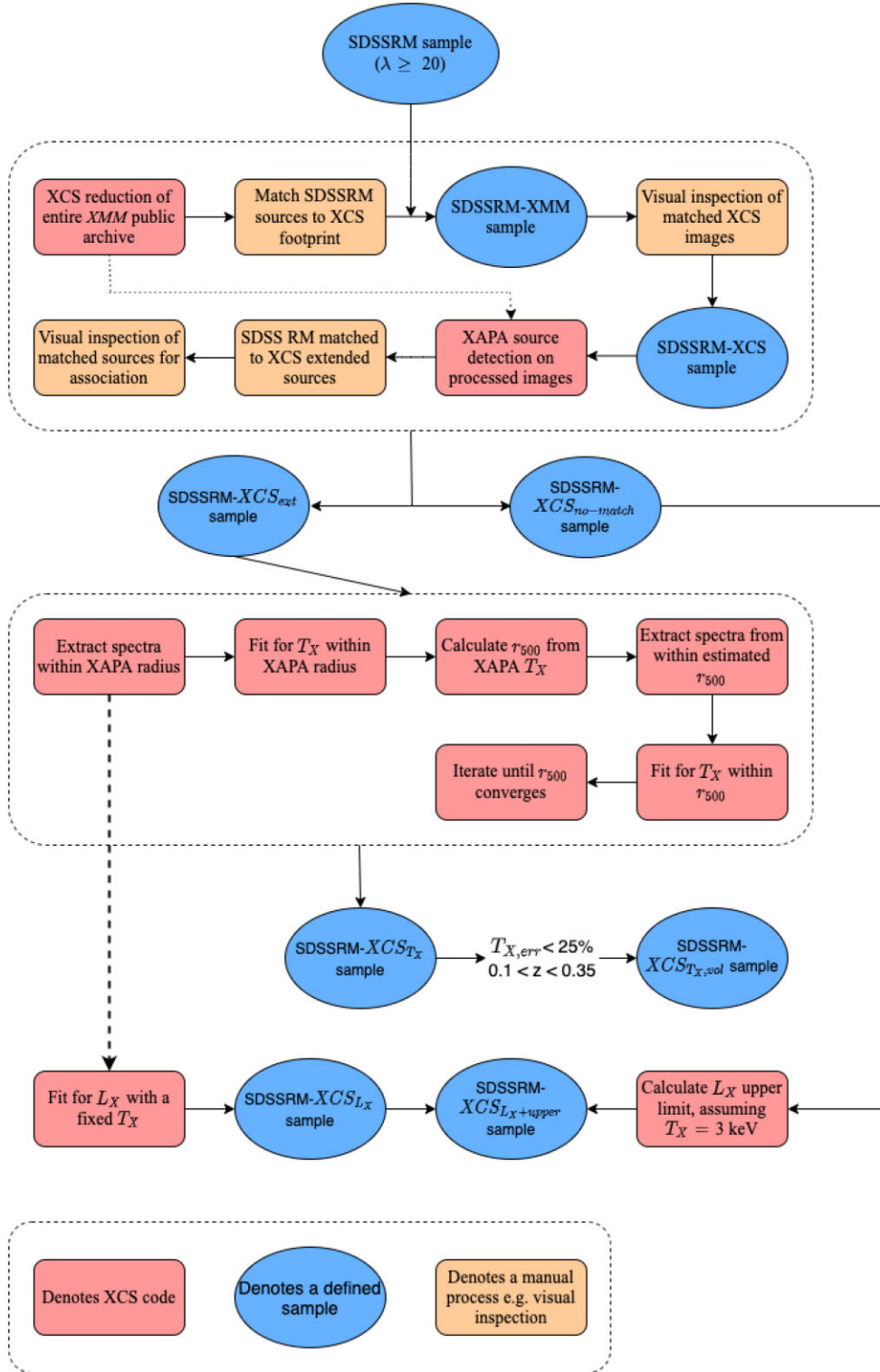
Figure 1. A flowchart outlining the process used to generate a sample of RM clusters with measured X-ray properties in the *SDSS* DR8RM footprint.

mission. This includes both those that were the intended target of the respective observation, and those that were detected serendipitously (e.g. in the outskirts of an *XMM* observation targeting a quasar). The XCS reduction process was fully described in Lloyd-Davies et al. (2011, hereafter LD11), but a brief outline is as follows.

The data were processed using *XMM*–SAS version 14.0.0, and events lists generated using the EPCHAIN and EMCHAIN tools. In order to exclude periods of high background levels and particle contamination, we generated light curves in 50s time bins in both the soft (0.1–1.0 keV) and hard (12–15 keV) bands. An iterative 3σ

Table 1. Summary of the SDSSRM cluster sub-samples produced during the matching process described throughout Section 2.

Sample	Brief description	# clusters	Relevant section
SDSSRM	SDSSRM DR8 clusters with a richness $\lambda_{RM} > 20$	66 028	Section 2.1
SDSSRM–*XMM*	SDSSRM clusters fall within the active area of one or more XCS processed *XMM* observations	1246	Section 2.3
SDSSRM–XCS	As above, but after visual inspection to remove matches to problematic *XMM* images	1189	Section 2.4
SDSSRM–XCS$_{ext}$	SDSSRM–XCS clusters that are matched to an *extended* XCS source	456	Section 2.4
SDSSRM–XCS$_{unm}$	SDSSRM–XCS clusters that are unmatched to an *extended* XCS source	733	Section 2.4.2

clipping process was performed on the light curves; time bins falling outside this range were excluded.

Single camera (i.e. PN, MOS1, and MOS2) images, along with the corresponding exposure maps, were then generated from the cleaned events files, spatially binned with a pixel size of 4.35 arcsec. The images and exposure maps were extracted in the 0.5–2.0 keV band, which is typical for soft-band X-ray image analysis. Individual camera images were merged to create a single image per observation, likewise the exposure maps. The MOS cameras were scaled to the PN during the merging by the use of energy conversion factors (ECFs) derived using the XSPEC (Arnaud 1996) package. The ECFs were calculated based upon an absorbed power-law model.

Using the merged images and exposure maps, we applied a bespoke WAVDETECT (Freeman et al. 2002) based source detection routine, the XCS Automated Pipeline Algorithm (XAPA). Once the source detection stage was complete, XAPA proceeded to classify the resulting sources as either point-like or extended. After removal of duplicates, a master source list (MSL) was generated. The MSL used in this work contained a total of 326 294 X-ray sources, of which 35 575 were classified as extended detections.

2.3 Identifying SDSSRM clusters in the XCS footprint

The SDSSRM cluster sample (Section 2.1) was compared to the footprint of the XCS image archive (Section 2.2). If a given RM centroid position fell within 15 arcmin of the aimpoint of one or more *XMM* observations, then that cluster was flagged as having a preliminary *XMM* match. The matched list was then filtered based upon the total exposure time, where the total exposure time is a combination of the exposure times for each of the PN, MOS1, and MOS2 cameras, defined as $0.5 \times PN_{exp} + 0.5 \times (MOS1_{exp} + MOS2_{exp})$. Only those clusters with a total mean exposure (defined within a 5 pixel radius centered on the RM position) of greater than 3 ks, and a median exposure of greater than 1.5 ks, were retained in the match list. The median exposure limit excluded RM clusters that had significant overlap with chip gaps or bad pixels. Next, an additional exposure (mean and median) filter was carried out at a position $0.8R_\lambda$ away from the RM defined centre (in the direction away from the *XMM* aimpoint). This was done to encapsulate the expected range of mis-centering between RM and XAPA centroids (see Zhang et al. 2019).

Based on these matching criteria, 1246 SDSSRM clusters fall within the active area of one or more XCS processed *XMM* observations. Hereafter, these 1246 SDSSRM clusters are referred to as the 'SDSSRM–*XMM*' sample (see Table 1). We then performed a visual inspection to remove clusters falling in observations with abnormally high background levels (e.g. Fig. A1a), and those that were corrupted due to proximity to a very bright point source[7] (e.g.

Fig. A1b). We removed 57 observations, therefore, after this filtering step, 1189 clusters remained. We denote this set as the 'SDSSRM–XCS' sample (see Table 1).

2.4 Cross-matching the SDSSRM–XCS sample with XCS extended sources

Although all 1189 SDSSRM–XCS clusters (Section 2.3) fall within the XCS defined *XMM* footprint of *SDSS*, this does not guarantee they are matched to an extended XAPA source. In this context, a match was defined to mean that the respective centroids were within $2\,h^{-1}$ Mpc of each other, where the distance was calculated assuming the RM cluster redshift. If more than one extended XAPA source met this criterion, we made the assumption that the closest (on the sky) match was the correct association. By this definition, 782 – of the input SDSSRM–XCS sample of 1189 – were initially matched to an extended XAPA source (the remaining, 407 SDSSRM–XCS entries are discussed further in Section 2.4.2).

The 782 XCS extended sources matched to SDSSRM clusters were then examined by eye to exclude cases where the X-ray emission was unlikely to be physically associated with the RM cluster in question. An example of a cluster that passed this test is shown in Fig. 2 (one that did not is shown in Fig. B1). The top left panel of Fig. 2 shows, with yellow circles, all the galaxies associated, by RM, with the cluster in question (other coloured circles depict the galaxies associated with other RM clusters in the field). In the bottom panel, the dashed circle highlights the position of the galaxy defined by RM as the most likely central galaxy. The 2nd, 3rd, 4th, and 5th most likely candidates, are highlighted by the yellow triangle, diamond, pentagon, and hexagon, respectively. The top right panel shows the *XMM* image of the matched XCS extended source. Following the visual inspection process, only 456, of the 782 checked, clusters were retained. These 456 are referred to hereafter as the 'SDSSRM-XCS$_{ext}$' sample, see Table 1 (the remaining 326 entries are discussed further in Section 2.4.2).

2.4.1 Accounting for incidences of redMaPPer mispercolations

The RM algorithm employs a process known a 'percolation' that aims to assign galaxies to the correct system when there are two or more RM clusters in close proximity on the sky (Rykoff et al. 2014, section 9.3). However, sometimes this process fails, with the result that RM assigns a low value of λ_{RM} to a genuinely rich cluster when it is close (in projection) to a less rich system, and vice versa. This RM failure mode is known as 'mispercolation' (see Hollowood et al. 2019). An example is shown in Fig. C1. The yellow circles in Fig. C1 (a) highlight the galaxies associated with a $\lambda_{RM} = 166$ RM cluster. From the distribution of the X-ray emission of the system (Fig. C1b), it is clear that the large richness has been incorrectly assigned to the low flux sub-halo of a nearby massive cluster (incorrectly assigned a richness of $\lambda_{RM} = 20$).

---

[7]Such sources produce artefacts in the *XMM* images including readout trails and ghost images of the telescope support structure.
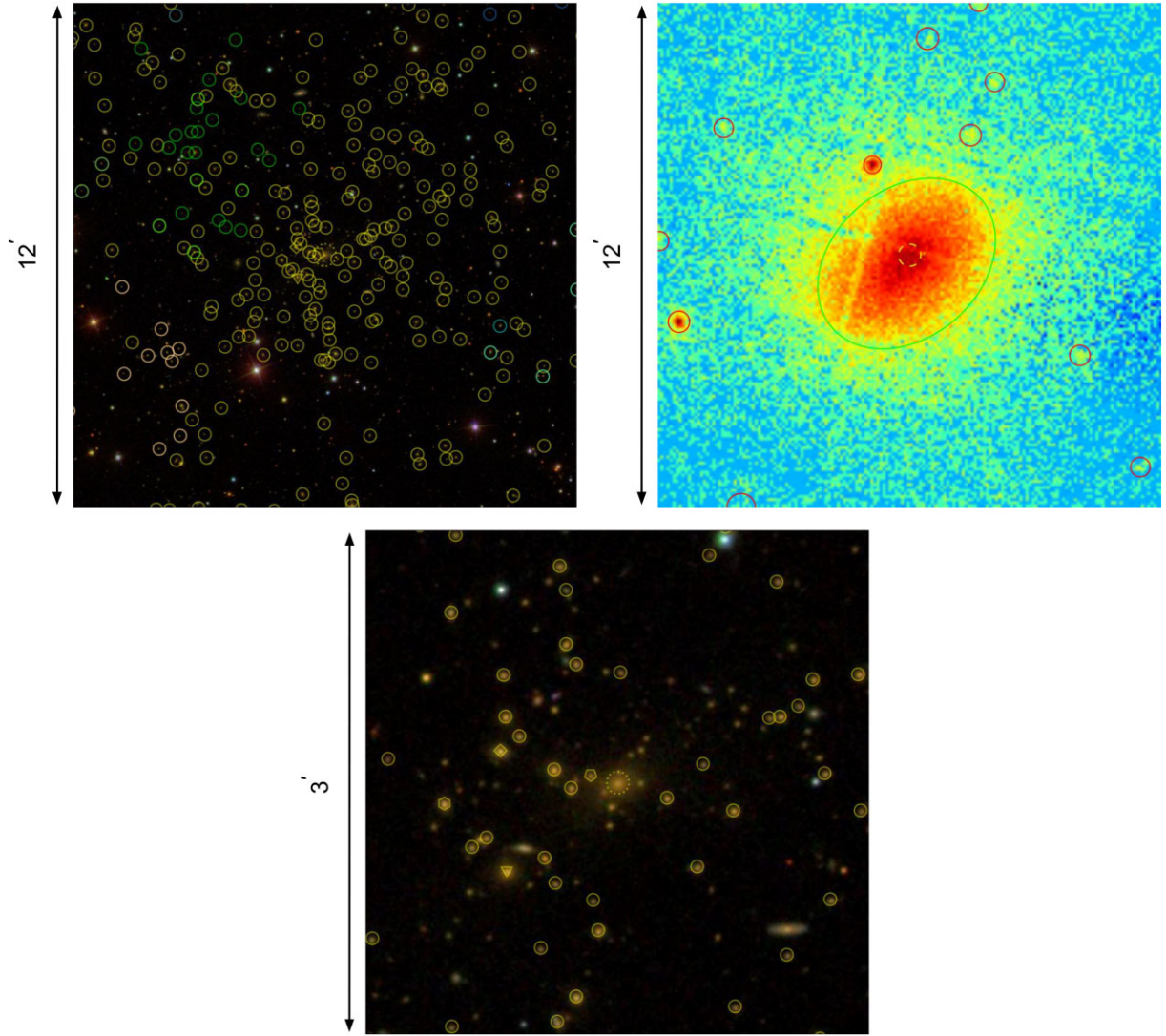
Figure 2. An example of a cluster in the SDSSRM–*XMM*$_{\text{ext}}$ sample (Table 1). Top left: *SDSS* optical image of the cluster XMMXCS J164020.2+464227.1 (*SDSS* RMID = 2), commonly referred to as Abell 2219, at a redshift of $z = 0.23$ and richness of $\lambda_{\text{RM}} = 199$. The dashed yellow circle and the other solid yellow shapes highlight the galaxies associated RMID = 2. Galaxy members of other nearby RM clusters nearby are circled in different colours (e.g. green, turquoise, and cream); Top right: *XMM* X-ray observation of the matched XCS extended source. Green (red) regions highlight extended (point) XAPA sources detected in the observation. Bottom middle: A zoom into the *SDSS* optical image. The yellow circle (dashed), triangle, diamond, pentagon, and hexagon represent, respectively, the 1st, 2nd, 3rd, 4th, and 5th most probable, according to the RM algorithm, candidate for the central galaxy.

During the visual inspection process that generated the SDSSRM-XCS$_{\text{ext}}$ sample (see Section 2.4), we identified three pairs of clusters affected by mispercolation. In order to correct their λ_{RM} values, we followed the method outlined in Hollowood et al. (2019), i.e. the originally assigned λ_{RM} value for the main halo was manually switched with that of the sub-halo. However, unlike Hollowood et al. (2019), we did not remove the lower flux system from further analysis if $\lambda_{\text{RM}} \geq 20$. Table C1 provides properties of the clusters effected by mispercolation. Of the 6 clusters effected by mispercolation, one is not included in the final SDSSRM-XCS$_{\text{ext}}$ sample, as its richness has a value of $\lambda_{\text{RM}} < 20$.

2.4.2 *SDSSRM*–XMM *entries not associated with XCS extended sources*

A total of 733 members of the SDSSRM–XCS sample are not included in the SDSSRM–XCS$_{\text{ext}}$ sample. This is because they have

not been matched to an XCS extended source. Of these, 407 are not close to any XCS extended source, whereas the remaining 326 were close in projection, but were deemed, after the eye-balling step, unlikely to be physically associated with it. Combined, these 733 'unmatched' clusters are denoted as the SDSSRM–XCS$_{\text{unm}}$ sub-set. For these clusters, we determine luminosity upper limits in Section 3.3 so that they can be included in the scaling relation analysis presented in Section 4.3.

To better understand why certain clusters were not detected in their respective *XMM* observation(s), we compared the distributions of their richness, off-axis distance, and redshift with those of the detected SDSSRM–XCS$_{\text{ext}}$ sample (see Fig. 3). Here, we defined the off-axis distance as the angular separation of the observation aim-point to the RM defined central galaxy: both the effective exposure time and the point spread function (PSF) degrade significantly with off-axis distance. To emphasize the redshift difference between the two samples, the points are colour coded by redshift. As expected,
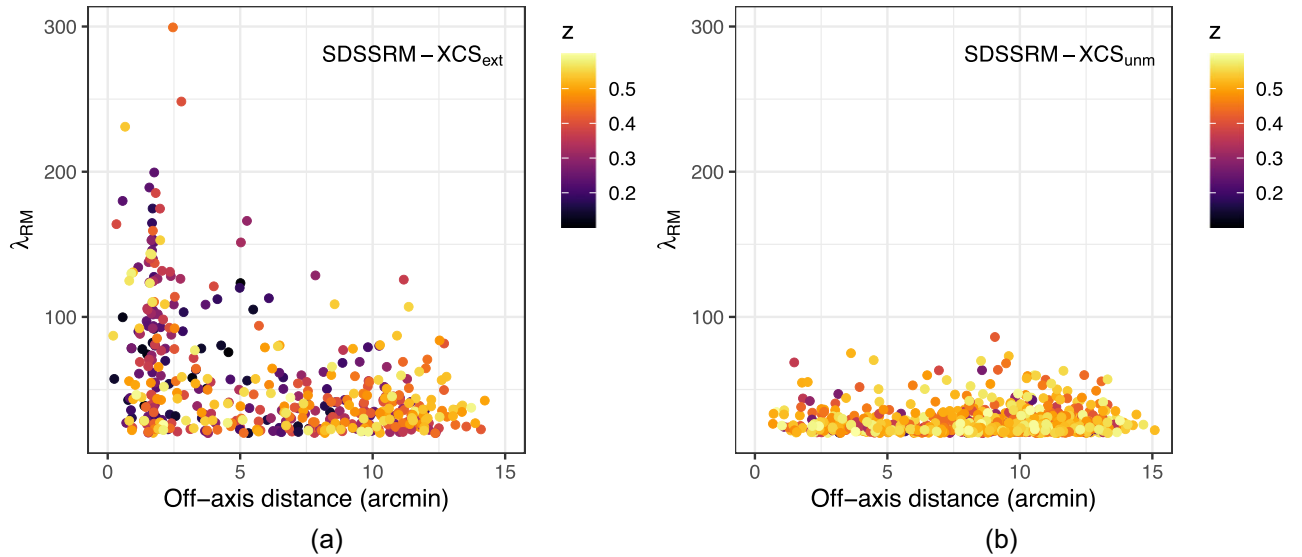
Figure 3. Distributions of richness (λ_{RM}) and off-axis distance for the SDSSRM–XCS$_{ext}$ (a) and SDSSRM–XCS$_{unm}$ (b) subsets. The off-axis distance is defined as the distance from the RM defined central galaxy to the centre of the *XMM* observation. In each case, the points are colour coded by redshift, given by the inset colourbar.

we find that the majority of SDSSRM–XCS$_{unm}$ clusters fall at larger off-axis positions, higher redshifts, and lower richnesses, than SDSSRM–XCS$_{ext}$ clusters.

2.5 False-positive rate

In order to determine the false-positive rate of matches between the *SDSS* DR8 catalogue and the XCS MSL, we make use of the SDSSRM random catalogue.[8] Full details of the construction of the random catalogue can be found in Rykoff et al. (2014, section 11). The random catalogue is constructed such as to map the detectability of clusters as a function of redshift and richness, taking into account the large-scale structure that is already imprinted on the galaxy catalogue. The random catalogue contains $\approx 3 \times 10^6$ clusters (which we denote as RMrd), a factor ~ 100 larger than the *SDSS* DR8 RM catalogue. We draw at random from the RMrd clusters and create samples of equal size to the *SDSS* DR8 RM catalogue (i.e. 66 028 clusters), resulting in 43 separate catalogues of RMrd clusters. For each separate catalogue, we first determined the number of RMrd positions falling on an *XMM* observation using the method described in Section 2.3 (i.e. a mean and median exposure cut of 3 and 1.5 ks respectively). We note that the RMrd clusters do not contain a R_λ estimate, therefore, we do not employ the additional exposure cut at a position $0.8R_\lambda$ away from the RM position (see Section 2.3). From the 43 mock catalogues, we determined that, on average, 1548 ± 33 RMrd clusters fell inside the *XMM* footprint. Next, we matched the RMrd clusters to XCS extended sources.

We defined a RMrd cluster to be associated with an extended source when the centroid fell within the XAPA detection region. Note that XAPA provides elliptical regions but, for this matching, we circularized the XAPA region by making the radius equal to the semimajor axis of the XAPA source. Fig. 4 shows the distribution of these associations for all 43 random catalogues. Based upon a Gaussian fit to the distribution, we find we would, on average, randomly match to an extended XAPA source 22.8 ± 5.0 times. We thus estimate
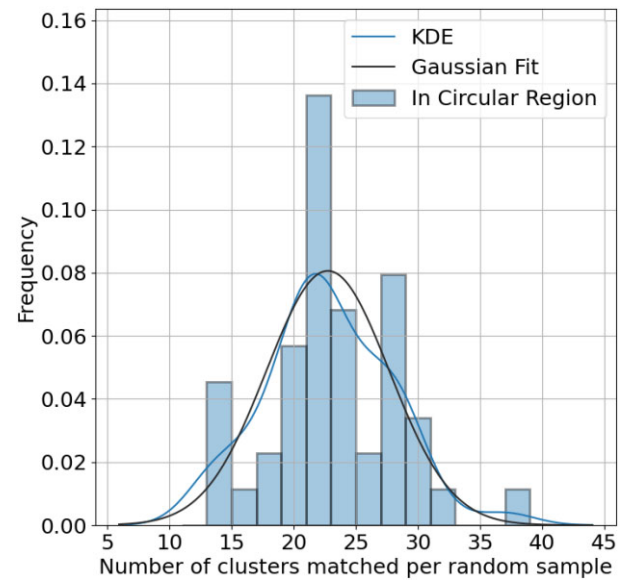
Figure 4. Distribution of the number of RMrd clusters matched to an extended XCS source, repeated using 43 samples of random positions created to match the size of the *SDSS* DR8 RM cluster sample (see 2.5).

a contamination rate in the SDSSRM-XCS sample of $\simeq 1.5$ per cent (23/1548). We note that since we made the simplifying assumption of a RMrd match when falling within a XAPA (circularised) region, and no eyeballing performed, this estimate is likely an upper limit.

3 X-RAY ANALYSIS OF THE SDSSRM–XCS SAMPLE

We used the XCS Post Processing Pipeline (XCS3P) to derive the X-ray properties of the SDSSRM–XCS$_{ext}$ clusters, i.e. their temperature (T_X) and luminosity (L_X). XCS3P can be run in batch mode and applied to hundreds of clusters at a time.

[8]http://risa.stanford.edu/redMaPPer/

A detailed description of XCS3P can be found in LD11, but a brief overview is as follows. Cluster spectra were extracted using the SAS tool EVSELECT and fit using XSPEC (Arnaud 1996). The fits were performed in the 0.3–7.9 keV band with an absorbed APEC model (Smith et al. 2001) using the *c*-statistic (Cash 1979). The APEC component accounts for the emission from a hot diffuse gas enriched with various elements. Relative abundances of these elements are defined as their ratio to Solar abundances ($Z_\odot$). The absorption due to the interstellar medium was taken into account using a multiplicative Tbabs model (Wilms, Allen & McCray 2000) in the fit, with the value of the absorption (n_H) taken from HI4PI Collaboration (2016) and frozen during the fitting process. The abundance was fixed at $0.3 Z_\odot$, a value typical for X-ray clusters (Kravtsov & Borgani 2012). The redshift was fixed to the value as determined by RM. We note that redshift uncertainties are not taken into account in the fit since the typical photometric redshift uncertainty for *SDSS* RM clusters is very small ($\frac{\sigma_z}{1+z} \leq 0.04$ out to a redshift of $z_\lambda = 0.6$, see fig. 9 in Rykoff et al. 2014). The APEC temperature and normalization were free to vary during the fitting process. Temperature errors were estimated using the XSPEC ERROR command, and quoted within 1σ. Finally, luminosities (and associated 1σ errors) were estimated from the best-fitting spectra using the XSPEC LUMIN command (in both the bolometric and 0.5–2.0 keV, rest frame, bands).

3.1 Updates to XCS3P since LD11

Improvements have been made to XCS3P since LD11 was published, and these are described in the sections below.

3.1.1 Spectral extraction region

In LD11, the spectral extraction region was based on the XAPA (see Section 2.2) characterized detection region i.e. an elliptical aperture defined using the lengths of the XAPA determined major and minor axes. The extraction region has since been updated to be within a circular overdensity radius (r_Δ). Overdensity radii are defined as the radius at which the density is Δ times the critical density of the Universe at the cluster redshift. We used two radii common in the X-ray cluster literature i.e. r_{500c} and r_{2500c}, where the radii were estimated using the relation given in Arnaud, Pointecouteau & Pratt (2005):

$$E(z)r_\Delta = B_\delta \left(\frac{T_X}{5\,\text{keV}} \right)^\beta , \qquad (1)$$

where $E(z) = \sqrt{\Omega_M(1+z)^3 + \Omega_\Lambda}$. In the case of r_{500c}, $B_\delta = 1104$ kpc and $\beta = 0.57$. The process is iterative because we do not know a priori what T_X is; an initial temperature was calculated within the XAPA defined elliptical source region, which is then used to estimate r_{500c} (using equation 1). A new T_X value was then measured from a spectrum extracted from a circular region with r_{500c} radius. The new T_X was then used to define a new r_{500c} value. The process was repeated until r_{500c} converged (the ratio of the new to old $0.9 > r_{500c, new}/r_{500c, old} < 1.1$). We employed the condition that at least three iterations were performed, regardless of the convergence. To account for the background in the spectral analysis, we made use of a local background annulus centred on the cluster, with an inner and outer radii of $1.05r_{500c}$ and $1.5r_{500c}$, respectively (see blue edged outer annulus in Fig. 6). It is also beneficial to compute core excluded properties for analysis (e.g. the use of core-excluded luminosities reduces the scatter in the luminosity–mass relation, see
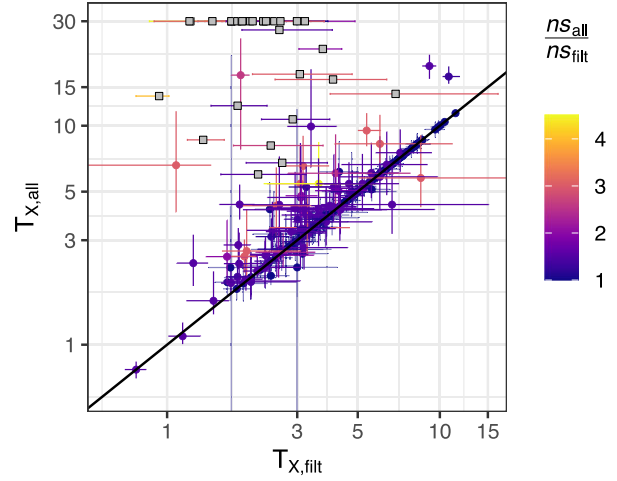
Figure 5. Comparison of the measured temperature when only including spectra in the simultaneous fit that pass quality controls ($T_{X, \text{filt}}$, Section 3.1.2), and the temperature when using all available spectra in the simultaneous fit ($T_{X, \text{all}}$, Section 3.1.2). Grey squares highlight clusters failing to converge during the iteration process (see Section 3.1.1) when determining $T_{X, \text{all}}$. The remaining clusters are colour coded by the ratio of the number of spectra when including all available spectra to the number passing the quality controls ($\frac{ns_{\text{all}}}{ns_{\text{filt}}}$). The black dashed line represents the 1:1 relation.

Mantz et al. 2018). Therefore, we repeat the process described above, but exclude the inner $0.15r_{500c}$ region (as used in many studies in the literature e.g. Pratt et al. 2009; Maughan et al. 2012; Lovisari et al. 2020).

In the r_{2500c} case, equation (1) was used, with $B_\delta = 491$ kpc and $\beta = 0.56$. The local background was taken into account using an annulus centred on the cluster with an inner and outer radius of $2r_{2500c}$ and $3r_{2500c}$, respectively. In all other respects, the derivation of $T_{X,2500}$ values followed that used for the $T_{X,500}$ values.

3.1.2 Selection of spectra

In the LD11 version of XCS3P, all available spectra were used in a siagreement between the two luminosity estimatesmultaneous XSPEC fit (ns_{all}). This included spectra derived from each of the three (PN, MOS1, and MOS2) *XMM* cameras and, where available, multiple *XMM* observations (up to 25 per cluster in some cases). However, we have subsequently discovered that using all available spectra, irrespective of data quality, can increase the measured temperature. This is demonstrated in Fig. 5 which compares the temperature estimated using all available spectra ($T_{X, \text{all}}$) to those determined by filtering out spectra that did not ($T_{X, \text{filt}}$), individually, produce a fitted temperature (complete with 1σ upper and lower limit values) in the range $0.08 < T_X < 20$ keV. The number of available spectra after filtering is defined as ns_{filt}. In Fig. 5, we plot $T_{X, \text{all}}$ against $T_{X, \text{filt}}$, with each point representing a cluster and colour coded by the ratio of the number of spectra used when determining $T_{X, \text{all}}$ and $T_{X, \text{filt}}$ (defined as $\frac{ns_{\text{all}}}{ns_{\text{filt}}}$). Grey squares indicate clusters that do not fulfill the criteria of a converged r_{500c} temperature for the $T_{X, \text{all}}$ analysis. Therefore, by using a filtered sample, we were able to extract more T_X values. Moreover, where $T_{X, \text{all}}$ and $T_{X, \text{filt}}$ differ, the former are typically higher. This suggests that there is residual background flaring in low signal-to-noise observations, because the particle background has a hard spectrum. For these reasons, XCS3P now only uses filtered spectra sets during the simultaneous fitting.

3.1.3 Measurement of luminosity uncertainties

When estimating the luminosity in XSPEC, the absorption component (n_H) must be set to zero in order to represent conditions at the cluster (i.e. unabsorbed). However, the luminosity uncertainties will be in error if they are also determined while n_H is set to zero, since the uncertainties are determined from the spectral fit to the absorbed data. This error was present in the LD11 version of XCS3P, and has now been corrected. In the latest version of XCS3P, the uncertainties are determined using an initial luminosity ($L_{\rm ini}$) calculation, before n_H has been set to zero. Then, n_H is set to zero and the luminosity extracted (L_0). The uncertainties are then scaled by the ratio of L_0 to $L_{\rm ini}$.

3.1.4 Exclusion of extended sources

The method used in LD11 to exclude nearby extended sources (NES) sometimes overestimated the area to 'drill out' around the NES, because the exclusion area was scaled by number of NES counts. Fig. 6 (left image) highlights the region used to exclude an NES in the LD11 analysis (red dashed ellipse). In this case, the excluded region overlaps with the source extraction region (green circle), removing a fraction of the source flux. Therefore, the scaling factor used in LD11 has been deprecated, see Fig. 6 (right image).

3.2 Luminosity estimates when T_X is fixed

Not all 456 clusters in the SDSSRM–XCS$_{\rm ext}$ sample yielded a reliable temperature measurement. However, it was still possible to estimate a luminosity value for them from the extracted spectra using an adapted version of the iterative procedure outlined in Section 3. In this adaptation, the temperature was fixed in the spectral fit. Initially, spectra were extracted within the XAPA defined region, and an XSPEC fit was performed with the T_X in the model fixed at 3 keV. This produced an initial luminosity value, which was fed into the luminosity–temperature relation presented in Section 4.1 (with parameters given in Table 3) to derive a more appropriate T_X value. An r_{500c} was estimated using equation (1) using this T_X value and a new spectrum was extracted and fit. The process was repeated until the change in the r_{500c} radius was less than within 10 per cent. Luminosities estimated in this way are denoted $L_{\rm Fixed\ Tx,52}^{r500}$. To test the validity of this method, we applied it to all clusters in the SDSSRM–XCS$_{\rm ext}$ sample, of which 351 have a measured L_X from the spectral extraction method described above (throughout Section 3). In Fig. 7, these luminosities (estimated using a fixed T_X) are compared to the luminosities estimated for the 381 clusters in the SDSSRM–XCS$_{T_X}$ sample (see Section 3.4, i.e. clusters where the luminosities were estimated from the spectral analysis with T_X free). The 1:1 relation is highlighted by the solid black line. This comparison shows there is a good agreement between the two luminosity estimates.

3.3 Upper limit estimates in the absence of an XCS detection

There are 733 SDSSRM–XCS clusters that have no corresponding confirmed match to an XCS extended source (the SDSSRM–XCS$_{\rm unm}$ sample, see Table 1). For these systems, we calculated upper limit luminosities in the following way. First, we assumed each RM cluster has a temperature of 3 keV and calculated r_{500c} using equation (1) (note, we only estimated upper limits within r_{500c}). We used a fixed temperature of 3 keV for the upper limit analysis to avoid bias coming from the correlation between the richness and luminosity (as would

happen if one were to estimate the temperature from $\lambda_{\rm RM}$). The choice of 3 keV was motivated by previous studies (e.g. Hollowood et al. 2019, who use 3 keV), and that the mean temperature of $\lambda_{\rm RM} \approx 20$–30 clusters in our SDSSRM–XCS$_{T_X,\rm vol}$ sample is 2.5 keV, close to our assumed value. The majority of the SDSSRM–XCS$_{\rm unm}$ clusters have $\lambda_{\rm RM} \approx 20$–30. We then measured a 3σ upper limit on the count-rate within those apertures, using the SAS tool EREGIONANALYSE, which implements the method of Kraft, Burrows & Nousek (1991). Point and extended sources are masked out from the analysis. The background region had radii with inner and outer values of $1.05r_{500c}$ and $1.5r_{500c}$, respectively.

In order to convert the count-rate upper limit into a luminosity upper limit, we used an energy conversion factor (ECF). First, an Auxiliary Response File (ARF) and Redistribution Matrix File (RMF) were produced at the position of the RM cluster, assuming the relevant overdensity radius. The ARF and RMF were then used to generate a fake spectrum in xspec using the FAKEIT tool. The process requires the use of a model with which to produce the fake spectrum, for which we assumed a TBABS × APEC model (the same one used to estimate cluster properties as in Section 3). We assumed an nH calculated at the RM position, the redshift as determined by RM, and the abundance fixed at $0.3\,Z_\odot$. The temperature was assumed to be 3 keV. An arbitrarily high exposure time, of 100 ks, was used to generate the spectrum. The ECF was then calculated as the ratio between the count-rate and the measured flux from the fake spectrum. Using this ECF, the count-rate upper limit is converted to a flux, and finally converted to a luminosity upper limit. Using this method, we measure upper limit luminosities for 599 of the SDSSRM–XCS$_{\rm unm}$ sample (representing ≈ 80 per cent of the input sample).[9]

### 3.4 Introducing the various SDSSRM–XCS sub-samples

In Table 2, we overview the various sub-samples of SDSSRM clusters that have been analysed in this work. The cluster sample that we use most (e.g. Sections 4.1, 4.2, and 5.1) is known as 'SDSSRM–XCS$_{T_X,\rm vol}$'. It contains 150 clusters that have accurate temperature estimates, defined as having an average percentage temperature error of $T_{X,\rm err} < 25$ per cent, and falling in the redshift range corresponding to the SDSSRM volume-limited sample (as estimated in Rykoff et al. 2014, $0.1 \leq z \leq 0.35$). The SDSSRM–XCS$_{T_X,\rm vol}$ sample is a subset of the SDSSRM–XCS$_{T_X}$ sample, which contains 381 clusters with $T_{X,\rm err} < 100$ per cent and no redshift limits imposed (see Section 4.3).

The largest sub-sample of SDSSRM clusters with measured luminosities is known as SDSSRM–XCS$_{L_X}$ and contains 456 clusters (no z limits imposed). In this case, the L_X values were estimated with a fixed (not fitted) T_X parameter (see Section 3.2). A subset of SDSSRM–XCS$_{L_X}$ clusters in the $0.1 \leq z \leq 0.35$ range has 178 entries and is known as SDSSRM–XCS$_{L_X,\rm vol}$.

Finally, the SDSSRM–XCS$_{L_X}$ sample is supplemented with upper limit luminosities determined for the SDSSRM–XCS$_{\rm unm}$ sample. These luminosities are added to the SDSSRM–XCS$_{L_X}$ sample to create a sample of 1055 clusters, which we denote as the SDSSRM–XCS$_{L_X+\rm upper}$ subset (no z limits). A subset of SDSSRM–XCS$_{L_X+\rm upper}$ clusters in the $0.1 \leq z \leq 0.35$ range has 222 entries and is known

---

[9]The remaining clusters could not have an upper limit measured since they fall on or near a chip gap, or the region was masked due to the presence of a point source or un-associated extended source
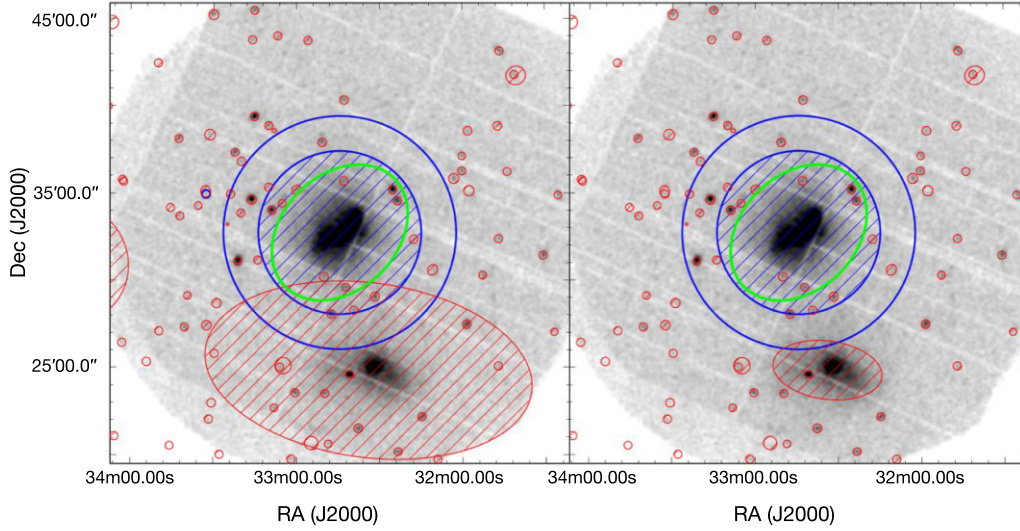
Figure 6. Updated approach to source masking in XCS3P compared to LD11. In each image the green ellipse represents the cluster extraction region, the blue edged annulus represents the background region and the red small circles are excluded point sources. The nearby extended source is excluded using the red hashed ellipse. In the LD11 analysis, the exclusion region was too large (left image). This has been corrected in the current version of XCS3P (right image, see Section 3.1.4).
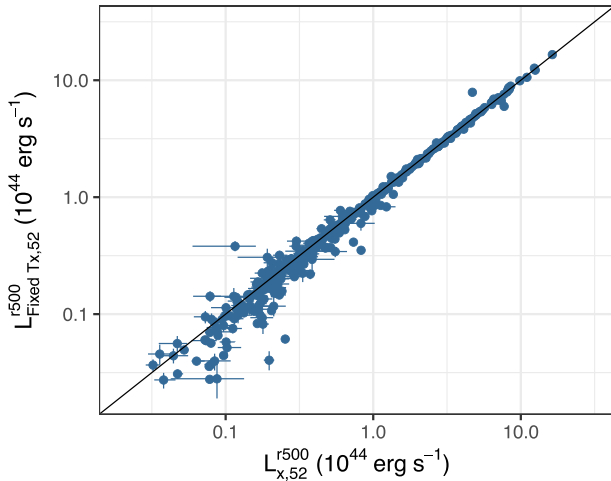
Figure 7. Comparison of luminosity determined using a fixed temperature ($L^{r500}_{\mathrm{Fixed\ Tx,52}}$) estimated from the luminosity temperature relation (see Section 3.2 for details), to that determined from spectra extracted within r_{500} (see Section 3). The solid black line indicates the 1:1 relation.

as SDSSRM–XCS$_{L_X + \mathrm{upper, vol}}$. This subset is used in the analyses presented in Section 4.3.

A data table containing properties for the cluster sample outlined in this work can be found at data table, along with a table description.

3.4.1 Comparison to the literature

3.4.1.1 Sample size We have delivered one of the largest cluster samples with coherently measured T_X values to date. The only equivalent sample is the XCS First Data release (XCSDR1; Mehrtens et al. 2012). XCSDR1 included 401 clusters with measured temperatures distributed across the entire extragalactic sky (i.e. extending beyond the SDSSDR8 footprint). In Fig. 8(a), we show the number of SDSSRM–XCS$_{T_X}$ clusters per T_X bin (the subset of 150 in the

SDSSRM–XCS$_{T_X, \mathrm{vol}}$ subsample is highlighted in blue). The T_X value distributions from a non-comprehensive list of other recently published samples are overplotted as spline curves, described by the following:

(i) The cyan curve shows the 57 *XMM* derived T_X values for *SDSS* DR8 RM clusters (spanning a redshift range of $0.14 < z < 0.59$) in the Molham et al. (2020, hereafter Mol20) sample. This sample is a subset of the X-CLASS catalogue (Clerc et al. 2012; Koulouridis et al. 2021).

(ii) The red curve shows the 95 *eROSITA* derived T_X values X-ray selected clusters (spanning a redshift range $0.049 < z < 0.708$) in the Liu et al. (2022, hereafter L22).[10] This sample is a subset of 542 clusters extracted from the 140 deg^2 contiguous *eROSITA* Final Equatorial-Depth Survey (eFEDS). We note that the eFEDS T_X values were derived from spectra extracted from a circular $r < 500$ kpc region, and that they have been scaled by a factor of 1.25 to account for the measured T_X offset between *eROSITA* and *XMM* (Turner et al. 2021).

(iii) The brown curve shows the 97 *Chandra* derived T_X values for SDSSRM clusters ($0.1 \le z \le 0.35$) in the Hollowood et al. (2019, hereafter H19)[11] sample. For the purposes of illustration, the *Chandra* T_X values are scaled to *XMM* using the calibration found in Rykoff et al. (2016).

(iv) The green curve shows the 120 *XMM* derived T_X values for *Planck* clusters (spanning a redshift range of $0.059 < z < 0.546$) in the Lovisari et al. (2020, hereafter L20).[12] This sample is a subset of the *Planck* Early Sunyaev–Zeldovich (Planck Collaboration VIII 2011) cluster catalogue.

(v) The yellow curve shows the 313 *XMM* and *Chandra* derived T_X values for X-ray selected clusters (spanning a redshift range $0.004 < z < 0.447$, with 70 per cent at $z < 0.1$) in the Migkas et al. (2020,

---

[10]Liu+21 sample
[11]Hollowood+ 19 sample
[12]Lovisari+ 20 sample

Table 2. Summary of the SDSSRM cluster sub-samples used for scaling relation analysis in this work.

Sample	Brief description	# clusters	Relevant sections
SDSSRM–XCS$_{T_X}$	SDSSRM-XCS$_{ext}$ clusters with a measured temperature value (with $T_{X,err} < 100$ per cent)	381	Section 3.4
SDSSRM-XCS$_{T_X,vol}$	As above, but limited to systems with $0.1 < z < 0.35$ and $T_{X,err} < 25$ per cent	150	Section 3.4
SDSSRM-XCS$_{L_X}$	SDSSRM-XCS$_{ext}$ clusters where the luminosity was measured assuming a fixed temperature	456	Section 3.2
SDSSRM-XCS$_{L_X,vol}$	As above, but limited to systems with $0.1 < z < 0.35$	178	Section 3.2
SDSSRM-XCS$_{L_X+upper}$	SDSSRM-XCS$_{L_X}$ sample, supplemented with upper limit luminosities	1055	Sections 3.2 and 3.3
SDSSRM-XCS$_{L_X+upper,vol}$	As above, but limited to systems with $0.1 < z < 0.35$	222	Sections 3.2 and 3.3
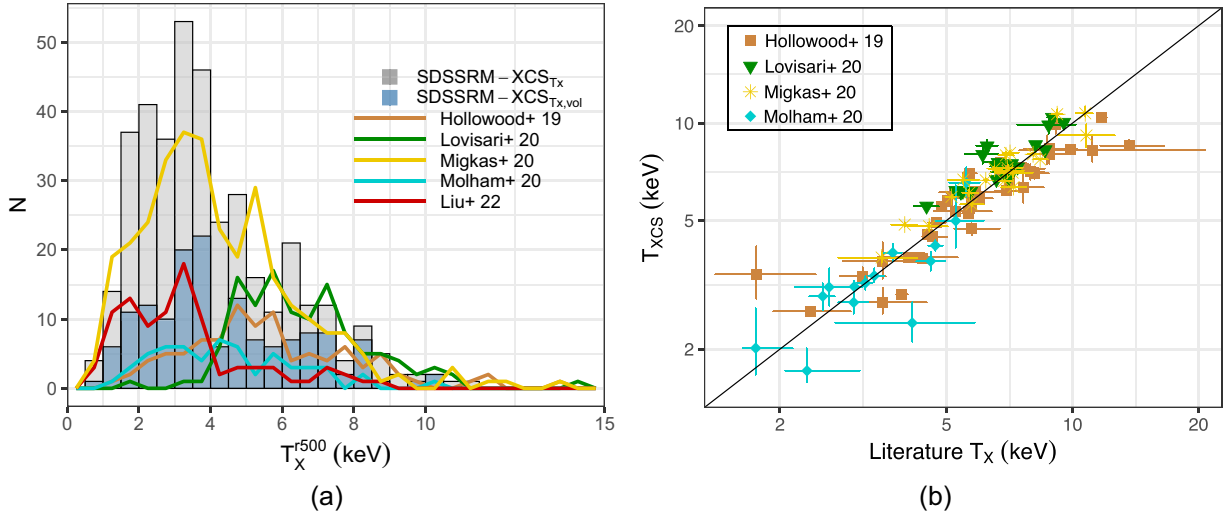
Figure 8. (a) Temperature distribution of the SDSSRM–XCS$_{T_X}$ (grey histogram) and SDSSRM–XCS$_{T_X,vol}$ (light blue histogram) samples. Distributions from Hollowood et al. (2019, brown line), Lovisari et al. (2020, green line), Migkas et al. (2020, yellow line), Molham et al. (2020, cyan line), and Liu et al. (2022, red line) are highlighted for comparison. Note that Hollowood et al. (2019) and Migkas et al. (2020) temperatures are scaled from *Chandra* to *XMM* using Rykoff et al. (2016) and Schellenberger et al. (2015), respectively, and the Liu et al. (2022) temperatures are scaled by the offset between *eROSITA* and *XMM* found in Turner et al. (2021). (b) Comparison of the measured temperatures in the SDSSRM-XCS$_{T_X,vol}$ sample to Hollowood et al. (2019, brown squares), Lovisari et al. (2020, green downward triangles), Migkas et al. (2020, yellow stars), and Molham et al. (2020, cyan diamonds), with 43, 20, 20, and 15 clusters in common, respectively. In most cases T_X^{r500} is compared, however, in the case of Migkas et al. (2020) we compare our $T_X^{(0.15-1)r_{500}}$ to their $T_X^{(0.2-0.5)r_{500}}$. The 1:1 relation is given by the black solid line.

hereafter Mig20) sample.[13] This sample is a subset of the Meta-Catalogue of X-ray detected Clusters of galaxies (MCXC; Piffaretti et al. 2011). We note that the *Chandra* values in Mig20 are scaled to *XMM* using Schellenberger et al. (2015, as used in Mig20), and that all 313 T_X values were derived from spectra extracted from a $(0.2–0.5)r_{500}$ region.

3.4.1.2 Temperature estimates To demonstrate the reliability of the T_X values estimated in this work, we have compared our values (using the SDSSRM–XCS$_{T_X,vol}$ sample) to those for clusters in common with the H19, L20, Mig20, and Mol20 samples mentioned above. There are 43, 20, 20, and 15 examples, respectively. For the purposes of this comparison, a *Chandra*-to-*XMM* scaling as been applied to the H19 and Mig20 T_X values as described above. Fig. 8(b) plots the comparison of the temperature for these three literature samples. The black line shows the 1:1 relation, highlighting both that the various T_X measurements are broadly consistent, and that the XCS values generally have smaller errors.

# 4 SCALING RELATIONS DERIVED FROM THE SDSSRM–XCS SAMPLES

In this section, we present the scaling relations derived from some of the SDSSRM–XCS samples described in Section 3.4 and Table 2. In Sections 4.1 and 4.2, we focus on the sample with the most robustly measured X-ray properties and that is restricted to the RM volume limited redshift range i.e. the SDSSRM–XCS$_{T_X,vol}$ cluster sample (see Section 3.4). In Section 4.3, we present fits to samples with less conservative cuts, to explore the relative importance of sample size over measurement accuracy. Fits to the scaling relations were performed in log space using the R package LInear Regression in Astronomy (LIRA)[14], fully described in Sereno (2016). Formally, scaling relations are fitted with a power law of the form

$$Y = A + B \cdot Z \pm \epsilon, \tag{2}$$

where $var(\epsilon) = \sigma_{Y|Z}^2$ and Z is the intrinsic cluster property. For simplicity, throughout, the scaling relations are denoted by the cluster

[13]Migkas+ 20 sample

[14]LIRA is available as an R package from https://cran.r-project.org/web/packages/lira/index.html
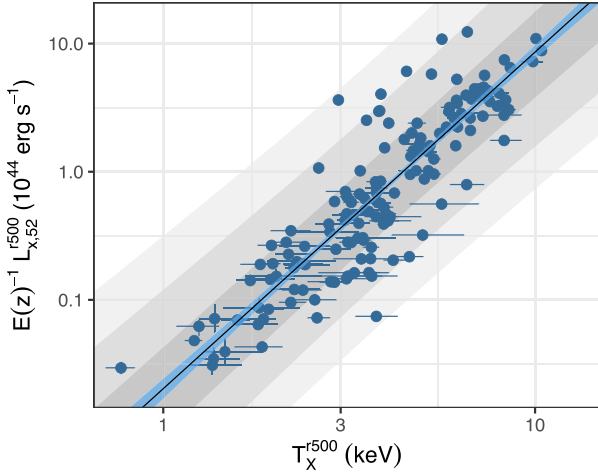
Figure 9. Luminosity–temperature relation of the SDSSRM–XCS$_{T_X, \text{vol}}$ subset (blue circles). The best fit to the data (see Section 4.1) is represented by the black solid line, and the light blue shaded region represents the 68 per cent confidence interval. The grey bands represent the 1σ, 2σ, and 3σ intrinsic scatter.

properties in question and the scatter given by σ (e.g. see equation 3). For these analyses we used core-included temperatures and soft band luminosities within r_{500c} unless otherwise stated. Temperature and luminosities estimated in this way are denoted T_X^{r500} and $L_{X,52}^{r500}$, respectively.

4.1 The luminosity–temperature relation derived from the SDSSRM–XCS$_{T_X, \text{vol}}$ sample

The $L_{X,52}^{r500}$–T_X^{r500} relation is shown in Fig. 9. The SDSSRM–XCS$_{T_X, \text{vol}}$ data points are shown as blue circles. A power-law relation between $L_{X,52}^{r500}$ and T_x^{r500} is fit to the data, which we express as

$$\log\left(\frac{L_{X,52}^{r500}}{E(z)^{\gamma_{LT}} L_0}\right) = \log(A_{LT}) + B_{LT} \log\left(\frac{T_X^{r500}}{T_0}\right) \pm \sigma_{L|T}, \quad (3)$$

where A_{LT} denotes the normalization, B_{LT} the slope, γ_{LT} the evolution with redshift, and $\sigma_{L|T}$ the intrinsic scatter. Note that the intrinsic scatter is given in natural log space and can be interpreted as the fractional scatter. We assumed $T_0 = 4$ keV, $L_0 = 0.8 \times 10^{44}$ erg s^{-1} (roughly the median values for the SDSSRM–XCS$_{T_X, \text{vol}}$ sample) and a self-similar evolution of the relation where $\gamma_{LT} = 1$. The fit to the SDSSRM–XCS$_{T_X, \text{vol}}$ sample is highlighted by the blue solid line in Fig. 9, with the lightblue shaded region representing the 68 per cent uncertainty. The grey bands represent the 1σ, 2σ, and 3σ intrinsic scatter. This scaling relation was used to estimate luminosities when the T_X was fixed, rather than fitted (see Section 3.2). The best-fitting LIRA parameters of the $L_{X,52}^{r500}$–T_X^{r500} relations are given in Table 3. For comparison, we performed a fit using the LINMIX routine (Kelly 2007), with best-fitting parameters also given in Table 3. Many literature studies using X-ray luminosities determine relations using the bolometric luminosity. Therefore, we also fitted the bolometric luminosity–temperature ($L_{X,bol}^{r500}$–T_X^{r500}) relation, with the best-fitting parameters from given in Table 3.

4.2 The X-ray observable–richness relations derived from the SDSSRM–XCS$_{T_X, \text{vol}}$ sample

The $L_{X,52}^{r500}$–λ_{RM} and T_X^{r500}–λ_{RM} relations for the SDSSRM–XCS$_{T_X, \text{vol}}$ (steel blue circles) are shown in Figs 10(a) and (b), respectively. We fit

for the $L_{X,52}^{r500}$–λ_{RM} and T_X^{r500}–λ_{RM} relations, again, which we express as

$$\log\left(\frac{L_{X,52}^{r500}}{E(z)^{\gamma_{L\lambda}} L_0}\right) = \log(A_{L\lambda}) + B_{L\lambda} \log\left(\frac{\lambda_{\text{RM}}}{\lambda_0}\right) \pm \sigma_{L|\lambda}, \quad (4)$$

$$\log\left(\frac{T_X^{r500}}{T_0}\right) = \log(A_{T\lambda}) + B_{T\lambda} \log\left(\frac{\lambda_{\text{RM}}}{\lambda_0}\right) \pm \sigma_{T|\lambda}, \quad (5)$$

where $A_{L\lambda}$ and $A_{T\lambda}$ denote the normalizations, $B_{L\lambda}$ and $B_{T\lambda}$ represent the slopes and $\sigma_{T|\lambda}$ and $\sigma_{L|\lambda}$ denote the intrinsic scatters (once again the values are given in natural log space). We assumed $L_0 = 0.8 \times 10^{44}$ erg s^{-1} in equation (4) and $T_0 = 4$ keV in equation (5), and in both relations assumed $\lambda_0 = 60$ (again, all roughly corresponding to the median values for the SDSSRM–XCS$_{T_X, \text{vol}}$ sample). Self-similar evolution for each relation is assumed such that $\gamma_{L\lambda} = 1$ in equation (4). We note that the $E(z)$ correction cancels out in the T_X–λ_{RM} relation [hence the absence of the $E(z)$ parameter in equation 5]. The best-fitting LIRA parameters for each relation are given in Table 3 (again, LINMIX parameters are also provided for comparison) and the best-fitting relations are given by the blue solid lines in Figs 10(a) and (b), with the 68 per cent uncertainty given by the light blue shaded region. The grey bands represent the 1σ, 2σ, and 3σ intrinsic scatter. A comparison of these results to those in the literature are presented in Section 4.4.

In summary, we find that the measured scatter of the L_X–λ_{RM} relation is roughly three times that of the T_X–λ_{RM}. This is not due to measurement error (indeed the percentage errors on the L_X values are much smaller than those on the T_X values) but likely because non-gravitational physics impacts the luminosity to a much greater extent than it does the temperature. Even expanding the sample of L_X values by a large factor (as will be possible with the eROSITA All Sky Survey; Predehl et al. 2021) will not bring the scatter down below that shown in Fig. 10(a).

4.3 Scaling relations with all available X-ray data

The SDSSRM–XCS$_{T_X, \text{vol}}$ sample only contains a fraction of the X-ray information available for SDSSRM–XCS clusters. In this section, we investigate whether there is a benefit to including additional clusters with less precise individual measurements.

To explore the impact of T_X measurement errors on the derived L_X–T_X relation (see Section 4.1), we have added all 381 clusters with a measured T_X value in the SDSS–XCS$_{T_X}$ sample. The results are shown in Fig. 11(a) and best-fitting parameters given in Table 3. It is clear that there is no significant change in the fitted relation when less accurate T_X values are included. There is some marginal benefit to including more clusters in the fit (e.g. the scatter drops a little, although not significantly).

To explore the impact of L_X measurement errors, and, to some extent, sample incompleteness, on the derived luminosity–richness relation, we make use of luminosities estimated with a fixed temperature (see Section 3.2) for all 456 clusters in the SDSSRM–XCS$_{\text{ext}}$ sample, combined with luminosity upper limits (Section 3.3) where available. The results are shown in Fig. 11(b) and best-fitting parameters given in Table 3. It is clear that when less accurate L_X values, and upper limits, are included that the measured scatter goes up a little, but does not change significantly. However, there are perceptible changes to the slope and normalization, which are likely a result of a combination of the change in L_X measurement method, and in the selection function.

In summary, it is probably worthwhile including all available T_X values when assessing T_X–λ scatter for cosmological studies, i.e. the

Table 3. Best-fitting parameters of the cluster scaling relations (see Sections 4.1 and 4.2 for details). For each relation, parameters are given for the SDSSRM-XCS$_{T_X,\mathrm{vol}}$ ($T_{X,err} < 25\%$ and $0.1 \leq z \leq 0.35$) cluster sample. Best-fitting parameters are given for the L_X–T_X, L_X–λ_{RM}, and T_X–λ_{RM} relations, given by equations (3), (4), and (5), respectively.

Relation (sample)	Fit	Normalization	Slope	Scatter	Figure
$L_{X,52}^{r500}$–T_X^{r500}		A_{LT}	B_{LT}	σ_{LT}	
SDSSRM–XCS$_{T_X,\mathrm{vol}}$	LIRA	0.97 ± 0.06	2.63 ± 0.12	0.68 ± 0.04	9
	LINMIX	0.98 ± 0.06	2.63 ± 0.12	0.69 ± 0.03	–
SDSSRM–XCS$_{T_X}$	LIRA	0.94 ± 0.04	2.49 ± 0.08	0.64 ± 0.03	11(a)
$L_{X,bol}^{r500}$–T_X^{r500}		A_{LbT}	B_{LbT}	σ_{LbT}	
SDSSRM–XCS$_{T_X,\mathrm{vol}}$	LIRA	3.05 ± 0.18	3.07 ± 0.12	0.68 ± 0.04	–
$L_{X,52}^{r500}$–λ_{RM}		$A_{L\lambda}$	$B_{L\lambda}$	$\sigma_{L\lambda}$	
SDSSRM–XCS$_{T_X,\mathrm{vol}}$	LIRA	0.98 ± 0.09	1.61 ± 0.14	1.07 ± 0.06	10(a)
	LINMIX	0.98 ± 0.09	1.62 ± 0.14	1.08 ± 0.06	–
SDSSRM–XCS$_{L_{X+\mathrm{upper}},\mathrm{vol}}$	LIRA	1.08 ± 0.10	1.84 ± 0.12	1.09 ± 0.06	11(b)
T_X^{r500}–λ_{RM}		$A_{T\lambda}$	$B_{T\lambda}$	$\sigma_{T\lambda}$	
SDSSRM–XCS$_{T_X,\mathrm{vol}}$	LIRA	1.01 ± 0.03	0.59 ± 0.04	0.33 ± 0.02	10(b)
	LINMIX	1.01 ± 0.03	0.59 ± 0.05	0.33 ± 0.01	–
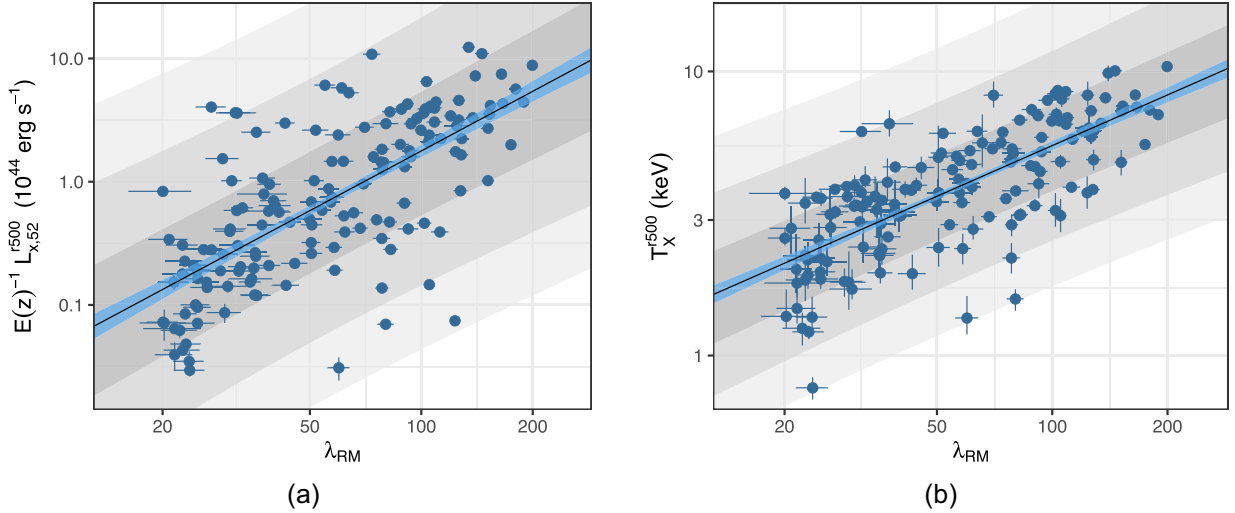
Figure 10. Luminosity–richness (a) and temperature–richness (b) relation of the SDSSRM–XCS$_{T_X,\mathrm{vol}}$. For each relation, the best fit to the data (see Section 4.2) is represented by the blue solid line, and the light blue shaded region represents the 68 per cent confidence interval of the mean logarithmic relation. The grey bands represent the 1σ, 2σ, and 3σ intrinsic scatter.

fitted parameters are robust to both measurement errors and selection effects. However, one should exercise more caution when using L_X–λ relations. The impact of selection on the L_X–λ relation will be explored in Upsdell et al. (preparation), which explores completeness and contamination in the low λ regime using an XCS analysis of contiguous *XMM* survey regions (totalling ∼57 deg^2) that overlap with the DES Year 3 data release (Abbott et al. 2018).

4.4 Comparison to the literature

Figs D1(b) and (d) demonstrate that T_X estimates values are insensitive to the details of the measurement process, be that the extraction aperture, or the inclusion of the cluster core. Furthermore, the comparisons in Fig. 8(b) show consistency of our measured T_X to those in the literature. Therefore, we can have confidence that comparisons of the T_X–λ scaling relations presented in Section 4.2 with those available in the literature will be meaningful. We do

not make similar comparisons to relation involving L_X since L_X estimates can vary significantly for a given cluster depending on the adopted methodology, see Figs D1(a) and (c). Furthermore, relations involving L_X are more dependent on sample selection than T_X.

We first compare to the T_X–λ_{RM} scaling relations presented in Rozo & Rykoff (2014, hereafter RR14). These are based on SDSSDR8 RM clusters ($0.1 < z < 0.3$), and so the λ values are consistent with those used herein. Two samples are presented in RR14, one contains 25 *XMM* derived T_X values taken from the first XCS data release (Mehrtens et al. 2012), hereafter the RR14$_{\mathrm{XCS}}$ sample. The other contains 54 *Chandra* derived T_X values, hereafter the RR14$_{\mathrm{ACCEPT}}$ sample. These 54 are a subsample of the 329 clusters in the ACCEPT data base (Cavagnolo et al. 2009). The input data vectors used in the RR14 are not available, therefore the comparison here is limited to the fitted relations (taken from table 2 of that paper). It is important to note that, for the ACCEPT sample, the RR14 fit was scaled to account for the offset in *Chandra* and *XMM* temperature measurements (using
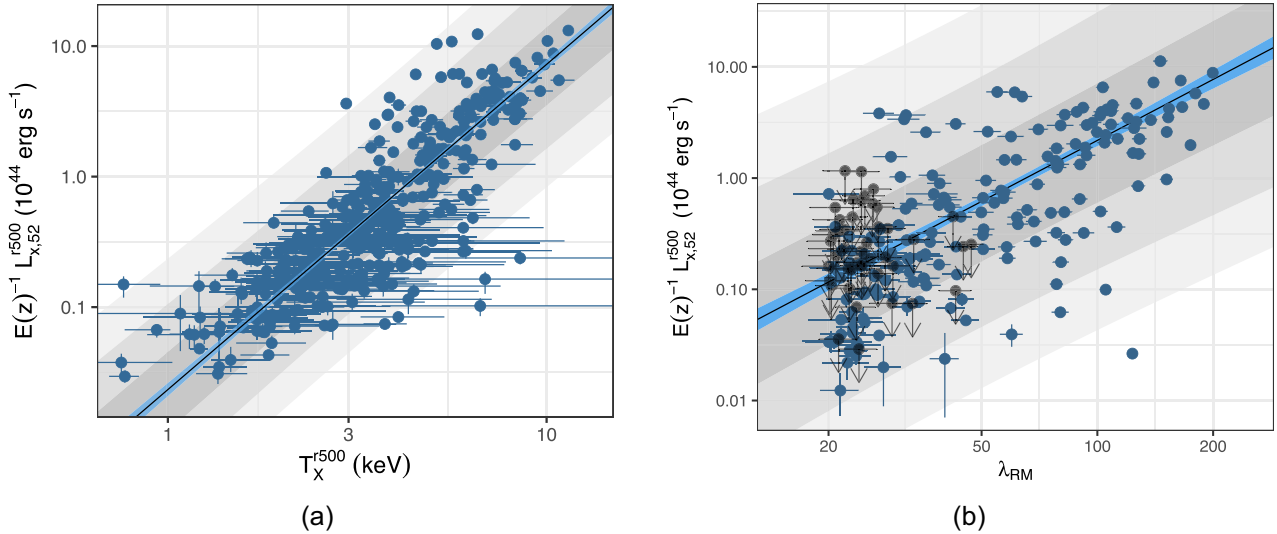
Figure 11. (a) Luminosity–temperature relation of the SDSSRM–XCS$_{T_X}$ sample (blue circles). The best fit to the data is represented by the black solid line, and the light blue shaded region represents the 68 per cent uncertainty. (b) Luminosity–richness relation of the SDSSRM–XCS$_{L_X+\text{upper,vol}}$ subset. Clusters are given by the blue points and luminosity upper limits for SDSSRM–XCS without an XCS detection given by the black circles (and downward arrows). The black solid line represents a fit to the data (including upper limits) with the light blue shaded region highlighting the 68 per cent uncertainty. In each plot, the grey bands represent the 1σ, 2σ, and 3σ intrinsic scatter.

Rykoff et al. 2016). As expected (given that the T_X methodology was very similar to that used herein), there is an excellent agreement in the case of the RR14$_{\text{XCS}}$ sample. The fit to the RR14$_{\text{ACCEPT}}$ sample is also consistent with that to the SDSSRM–XCS$_{T_X,\text{vol}}$ sample. However, as can be seen in Fig. 12(a), the slope is steeper (although at $<3\sigma$). There is consistency in normalization at the pivot point ($\lambda_0 = 60$). This contrary to that found in RR14, who found an ≈ 40 per cent difference between their fits to RR14$_{\text{ACCEPT}}$ and to R14$_{\text{XCS}}$ because RR14 did not carry out any *Chandra* to *XMM* T_X scaling.

In Fig. 12(b), we compare our T_X–λ scaling relation to that derived from the H19 sample of 97 SDSSRM clusters (brown curve/points in Fig. 8). In this case, the input data vector was available, so we were able to perform a new fit following the approach in Section 4.2, i.e. with $\lambda_0 = 60$ and $T_0 = 4$ keV, to maximize uniformity in the method. The comparison of the data and fits is given in Fig. 12(c, with the appropriate *Chandra* and *XMM* T_X scaling applied). The H19 data are given by the brown squares, with the LIRA fit given by the brown dashed line (and brown shaded region highlighting the 68 per cent uncertainty). We obtain fit parameters of the normalization and slope of $A_{T\lambda,H19} = 1.16 \pm 0.04$ and $B_{T\lambda,H19} = 0.50 \pm 0.05$, respectively. There is a small (14 per cent) offset in normalization at the pivot point ($\lambda_0 = 60$) significant at the 2.9σ level. While not significant, we assess the impact of the choice of *Chandra*-to-*XMM* temperature scaling on the above comparison. Therefore, we rescaled the H19 temperatures to *XMM* using the scaling found in Schellenberger et al. (2015) and re-fit the H19 T_X–λ relation. We obtain fit parameters of $A_{T\lambda,H19} = 1.23 \pm 0.03$ and $B_{T\lambda,H19} = 0.44 \pm 0.05$. The offset in normalization increases to ≈ 20 per cent, significant at the 5.1σ level. This highlights the potential difficulty of combining *Chandra* and *XMM* data. However, we note, one cannot exclude the effects of differences in selection between the two archival samples.

In Fig. 12(c), we compare our T_X–λ scaling relation to that based on the CAMIRA analysis of Hyper Suprime-Cam (HSC) observations (Oguri et al. 2018). The CAMIRA algorithm is similar to RM, in that it identifies clusters using the red sequence, but the estimated richness values will differ. The T_X–λ scaling relation analysis based

on 50 CAMIRA clusters is presented in Oguri et al. (2018), where the input T_X values were derived from *XMM* observations. For these 50 clusters, 34 T_X values were taken from Giles et al. (2016) and 16 T_X values taken from Clerc et al. (2014). Again, we were able to refit the input data using the approach in Section 4.2, as they were kindly made available to us via private communication by the authors. We obtain fit parameters of the normalization and slope of $A_{T\lambda,O18} = 1.04 \pm 0.10$ and $B_{T\lambda,O18} = 0.56 \pm 0.11$, respectively. Fig. 12(d) compares the SDSSRM–XCS$_{T_X,\text{vol}}$ T_X–λ_{RM} relation and the fit to the CAMIRA data (given by the purple diamonds with the best-fitting relation given by the purple dashed line and light purple shaded region the 68 per cent uncertainty). We note that richness is defined as N_{mem} in Oguri et al. (2018), but we keep the notation of λ_{RM} in Fig. 12(c) for clarity in the comparisons. As seen in Fig. 12(c), the two relation are fully consistent, albeit with the caveat that $\lambda_{\text{RM}} \neq N_{\text{mem}}$.

Finally, we compare to the T_X–λ_{RM} scaling relations presented in Farahi et al. (2019, hereafter F19). The relations are constrained using RM clusters detected within 1500 deg^2 of the DES (using the 1st yr of DES observations Drlica-Wagner et al. 2018). DES RM clusters were matched to *XMM* detected clusters using the same processes outlined in this work, resulting in a sample of 110 clusters used for the T_X–λ_{RM} scaling analysis. The clusters fall within $0.2 < z < 0.7$ and do not contain a temperature error cut (unlike in the SDSSRM–XCS$_{T_X,\text{vol}}$ sample). Furthermore, the temperatures are determined within r_{2500}. The input data vector was obtained, and the T_X^{2500}–λ_{RM} relation fit following Section 4.2 i.e. with $\lambda_0 = 60$ and $T_0 = 4$ keV. The comparison of the data and fits are given in Fig. 12(d). The F19 data are given by the dark-red triangles, with the LIRA fit given by the dark-red dashed line (and red shaded region the 68 per cent uncertainty). The SDSSRM–XCS$_{T_X,\text{vol}}$ relation is mostly obscured by the F19 fit, because the results are so consistent.

In summary, the results presented here (and in Section 3.4.1) are consistent with those in the literature and based on the largest compilation of T_X and λ_{RM} data to date. Furthermore, the extremely consistent comparison between this work and the results in F19
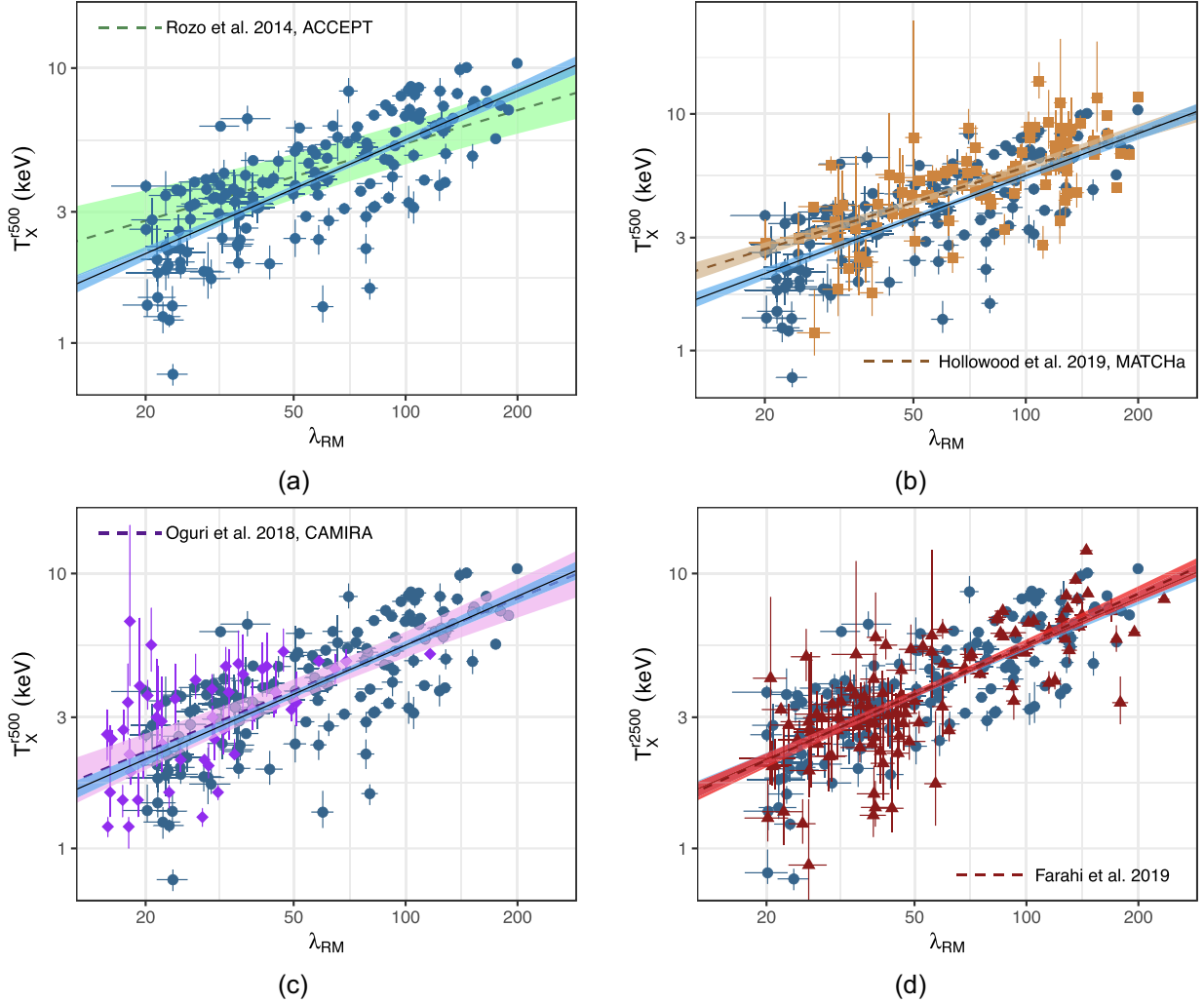
Figure 12. Comparison of the SDSSRM–XCS$_{T_X,\mathrm{vol}}$ temperature–richness relation to previously published relations. In each case, the black solid line represents a fit to the SDSSRM–XCS$_{T_X,\mathrm{vol}}$ data (as given in Table 3) and the light blue shaded region the corresponding 68 per cent uncertainty. Comparison to the fit provided in Rozo & Rykoff (2014, green dashed line and light green shaded region highlighting the 68 per cent uncertainty) using the R14$_{\mathrm{ACCEPT}}$ sample (note the relation has been scaled to *XMM* temperatures using Rykoff et al. 2016) is shown in (a). Comparison to the data given in Hollowood et al. (2019) is show in plot (b), scaled to *XMM* temperatures using Rykoff et al. (2016), with the LIRA fit to the data given by the brown dashed line and the 68 per cent uncertainty given by the brown shaded region. Comparison to the data given in Oguri et al. (2018) is shown in plot (c), with the LIRA fit to the data given by the purple dashed line and 68 per cent uncertainty given by the light purple shaded region. Note, the richness is estimated from CAMIRA, denoted $N_{\mathrm{mem(CAMIRA)}}$. Comparison to the data given in Farahi et al. (2019, dark-red triangles) is shown in plot (d), with the LIRA fit given by the dark-red dashed line and the 68 per cent uncertainty given by the red shaded region (note the agreement between the fits obscures much of the comparison, and in this case the T_X values were measured in a r_{2500} apertures).

(Fig. 12d), highlights that our sample can be combined with clusters from the DES for further analysis (see further discussion in Section 5.2).

5 DISCUSSION

As mentioned above (see Section 3.4), we have compiled one of the largest samples of consistently derived T_X values to date. This allows us to explore factors that might influence measured (as opposed to intrinsic) scaling relations. For example, in Section 5.1, we explore the impact of selection on the relations, specifically the difference between targeted and serendipitous detections. And, in Section 5.2, we investigate the recent claims of an anisotropy across the sky in the measured L_X–T_X relation (Migkas et al. 2020).

5.1 The dependence of scaling relations on detection type (targeted or serendipitous)

We have separated the SDSSRM–XCS$_{T_X,\mathrm{vol}}$ clusters into those that were the target of their respective *XMM–Newton* and those that were detected 'serendipitously'. The classification was done based upon a visual inspection of the X-ray images and information from the *XMM–Newton* Science Archive (namely the target name and target type). Of the 150 SDSSRM–XCS$_{T_X,\mathrm{vol}}$ clusters, 97 were flagged as being *XMM–Newton* targets, and 53 as serendipitous detections. We then revisited the scaling relations presented in Table 3. The results are presented in Table 4, plotted in Figs 13(a), 14(a) and (b). In all cases, the measured normalization of the targeted sub-sample is higher than that of the serendipitous sub-sample (ranging between 2.9σ and 5.1σ). This remains true even when the emission from

Table 4. Best-fitting parameters of the cluster scaling relations for the SDSSRM-XCS$_{T_X,\text{vol}}$ cluster sample, split between the targeted and serendipitous sub-samples (as defined in Section 5.1). Best-fitting parameters are given for the L_X–T_X, L_X–λ_{RM}, and T_X–λ_{RM} relations, given by equations (3), (4), and (5), respectively.

Relation (sample)	Fit	Normalization	Slope	Scatter	Figure
$L_{X,52}^{r500}$–T_X^{r500}		A_{LT}	B_{LT}	σ_{LT}	
SDSSRM–XCS$_{T_X,\text{vol}}$					
Targets	LIRA	1.04 ± 0.09	2.63 ± 0.20	0.74 ± 0.06	13(a)
Serendipitous	LIRA	0.66 ± 0.09	2.00 ± 0.22	0.52 ± 0.06	13(a)
$L_{X,52}^{r500}$–λ_{RM}		$A_{L\lambda}$	$B_{L\lambda}$	$\sigma_{L\lambda}$	
SDSSRM–XCS$_{T_X,\text{vol}}$					
Targets	LIRA	1.42 ± 0.16	1.13 ± 0.19	1.06 ± 0.07	14(a)
Serendipitous	LIRA	0.48 ± 0.09	1.23 ± 0.27	0.79 ± 0.08	14(a)
T_X^{r500}–λ_{RM}		$A_{T\lambda}$	$B_{T\lambda}$	$\sigma_{T\lambda}$	
SDSSRM–XCS$_{T_X,\text{vol}}$					
Targets	LIRA	1.14 ± 0.03	0.45 ± 0.05	0.27 ± 0.02	14(b)
Serendipitous	LIRA	0.81 ± 0.06	0.50 ± 0.12	0.34 ± 0.04	14(b)

the cluster cores is excluded, see Table D1, Figs 13(b), 14(c) and 14(d). While the measured slope of the $L_{X,52}^{r500}$–T_X^{r500} differs, it is only significant at the $\approx 2\sigma$ level. There is very little change in the richness scaling relations.

The current data are not sufficient to draw a firm conclusion as to the cause of these differences. However, they are unlikely to be due to a systematic in the XCS analysis methods, i.e. whereby biases in measured L_X or T_X values are correlated with location on the detector: LD11 studied the effect of measuring temperatures for the same clusters that were detected at a high off-axis position and then re-observed at the on-axis aimpoint. LD11 found a 1:1 relationship between the measured temperatures, finding no systematic offset (see fig 18 in LD11).

Instead, we suggest the cause is due to incompleteness in the sub-samples. There is a dearth of X-ray bright objects in the serendipitous sub-sample because these clusters are intrinsically very rare and so have a low projected sky density: a small area serendipitous survey is unlikely to come across them by accident. In the targeted sample, many *XMM* (and *Chandra*) targets were historically drawn from samples detected by the *ROSAT* All-Sky Survey (which had a relatively bright flux limit) and followed-up clusters with a high luminosity. Fig. A1 in Mantz et al. (2010) demonstrates how biases (specifically a luminosity limit) can significantly flatten the measured slope of a scaling relation. In addition, both sub-samples are incomplete at the low flux end due to biases in selection. It is possible to model the impact of incompleteness (as was done in Mantz et al. 2010) but is beyond the scope of this work. The true normalization and slope of the L_X–λ relation should be uncovered by the X-ray selected samples from the eRASS project, but in the meantime it would be prudent to use only T_X–λ relations for cosmological studies (as these are the least impacted by the sub-sample choice, see Figs 14b and d).

5.2 Investigating L_X–T_X isotropy with the *SDSS*–XCS$_{\text{ext}}$ sample

Recently, Mig20 made a claim relating to a possible anisotropy across the sky in the luminosity–temperature relation (Migkas et al. 2020). This claim, if true, would add additional systematics and uncertainty when using cluster number counts as a cosmological probe. The main Mig20 result was based on 313 clusters with measured T_X values (the yellow curve in Fig. 8a). These 313 are made up of

a compilation of both *XMM* and re-scaled *Chandra* T_X values. So we felt it was worthwhile to re-explore the Mig20 result using the larger (381) SDSSRM–XCS$_{T_X}$ sample of clusters, with T_X values drawn only from one telescope. Additional motivation comes from the results presented in Section 5.1, the difference in normalization seen in Fig. 13 is larger than that presented in Mig20. Note that while we focus on the results of Mig20 using the 313 clusters, the conclusions of Mig20 were enhanced by using this main sample and a combination of clusters from the ACC (Horner 2001) and XCS-DR1 (Mehrtens et al. 2012).

To demonstrate the robustness of our technique, we first repeated the analysis presented in Mig20, using the same input data vectors. In brief, the method is as follows: The sky is binned into regions over the full range of galactic longitude (l) and latitude (b), using a bin width of $\Delta l = 1°$ and $\Delta b = 1°$ (creating 65 160 bins on the sky). At the centre of each bin, a cone with a radius θ is used to find a subset of all clusters within an angular separation of θ_d from the coordinates of the bin. Using this subset, the 'local' L_X–T_X relation is fit using LIRA, following the same method as described in Section 4.1. However, as per Mig20, the slope of the local relation is fixed at all-sky value. A statistical weighting is applied to each cluster in the subset by increasing the size of the uncertainties by a factor

$$\cos\left(\frac{\theta_d}{\theta} \times 90°\right). \qquad (6)$$

At each position on the sky, the local L_X–T_X normalization, A, is divided by the normalization of the all sky L_X–T_X relation (A_{all}), with sky maps plotted based upon A/A_{all}. In Fig. E1(a), we replicate the results presented in Mig20 fig. 8 for the $\theta = 60°$ cone (thus confirming that our method is robust). This test also shows that the dipole feature is present irrespective of the linear regression fitting method used. Whereas we used LIRA, the Mig20 analysis used a fitting method equivalent to the BCES Y|X fitting method (Akritas & Bershady 1996).

We then apply the same method to the SDSSRM–XCS$_{T_X}$ sample. Note we use core excluded properties for this, in line with Mig20, who used $(0.2$–$0.5)r_{500}$ values. The ratio of A/A_{all} over the sky is then determined where there are >30 clusters in the bin. Figs 15(a) and (b) display the sky distribution of A/A_{all}, assuming cones of $\theta = 60°$ and $\theta = 75°$, respectively. The $\theta = 60°$ cone was chosen, as the dipole feature found in Mig20 is the most prominent at this
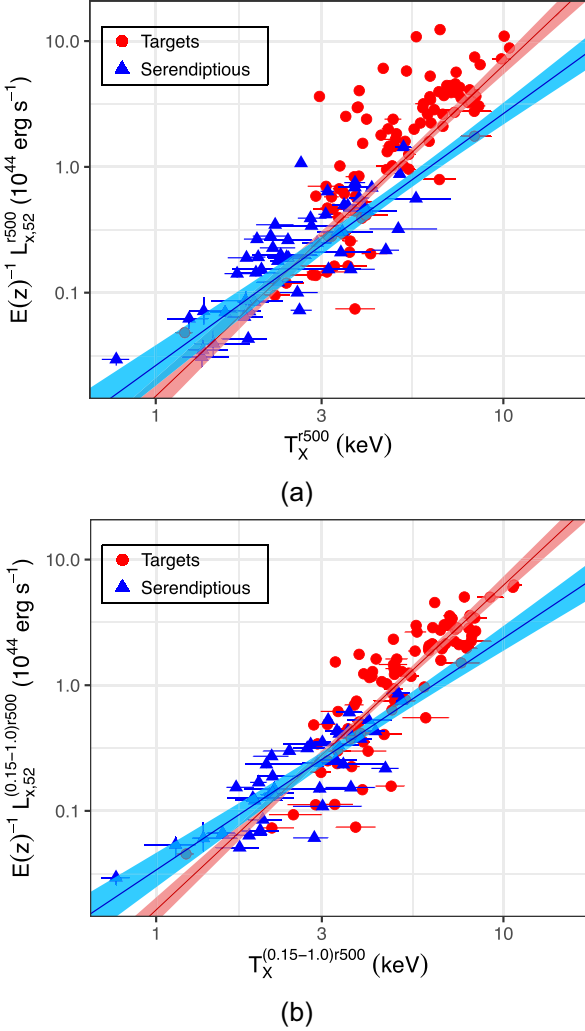
Figure 13. Luminosity–temperature relation of the SDSSRM-XCS$_{T_X,\text{vol}}$ sample, split between targeted (red circles) and serendipitous (blue triangles) clusters. The fiducial core-included r_{500} relations are shown in Plot (a, $L_{X,52}^{r500}$–T_X^{r500}), and the core-excluded relation in Plot (b, $L_{X,52}^{(0.15-1)r500}$–$T_X^{(0.15-1)r500}$). The red and blue lines represent a fit to the targeted and serendipitous clusters, respectively (fit using equation 3). The shaded regions around the respective lines represents the 68 per cent confidence interval of the mean logarithmic relation.

scale. The $\theta = 75°$ cone was chosen to increase the sky coverage. Based upon the distribution of A/A_{all} (Fig. 15), we do not observe the anisotropy feature found in Mig20 for the $60°$, although for the $75°$ we start to see hints of a decrease in A/A_{all}, coincident with the position of the isotropy feature found in Mig20. However, it is not possible to yet confirm the existence of an anisotropy feature because there is a region in the Southern sky where we are not able to measure A/A_{all} because *SDSS* is a northern survey. The strong edge features around the empty area correspond to local regions where all clusters in the respective cones have an angular separation of $\geq 55°$. Assuming equation (6), and $\theta_d > 55°$, the uncertainties on the measured cluster properties are divided by ≤ 0.13. The resulting local L_X–T_X relation thus becomes unconstrained. We therefore test the use of a new error scaling method as given in Migkas et al. (2021). The updated error scaling in Migkas et al. (2021) follows the form $\cos(\theta/90°)$, and is noted as a more conservative scaling approach.

Furthermore, we apply another update given in Migkas et al. (2021), where the slope of the local L_X–T_X relation is left free to vary (as opposed to being fixed as in Mig20). The results of these updates are presented in Fig. E1(b). The edge feature around the empty area appears less scattered, however, again due to this empty feature, no anisotropy feature is observed.

In summary, while our sample size is larger than the one presented in Mig20, and we have replicated the results using Mig20 data, further data are required due to the *SDSS* sky coverage. For this, the sample used here will be combined with RM clusters detected from the DES Y3 Gold catalogue (Sevilla-Noarbe et al. 2021) to improve the sky coverage. This technique (of combining *SDSS* and DES RM clusters) has been successfully applied in Wetzell et al. (2022) to measure the correlations between velocity dispersion, λ_{RM}, T_X, and L_X for RM clusters. The results shown in Fig. 12(d) also give us confidence that *SDSS* and DES cluster samples can be jointly analysed.

6 SUMMARY

In this paper, we detail the X-ray analysis of SDSSRM clusters using data products from the XMM Cluster Survey (XCS). In summary:

(i) In total, 1189 SDSSRM clusters fall within the cleaned *XMM–Newton* footprint. This has yielded 456 confirmed detections accompanied by X-ray luminosity (L_X) measurements. Using an updated version of the XCS Post Processing Pipeline (XCS3P), we have extracted 381 X-ray temperature measurements (T_X) from these 456 clusters. This represents one of the largest samples of coherently derived cluster T_X values to date. We have also shown that the reliability of derived T_X values improves when low quality spectra are removed from joint fits.

(ii) We find that the SDSSRM clusters in the *XMM* footprint that were not detected are primarily lower richness systems (75 per cent at $\lambda < 30$). It was possible to estimate L_X upper limits for most 599 (of 733) of these non-detections.

(iii) Our analysis of the X-ray observable to richness scaling relations has demonstrated that scatter in the T_X–λ relation is roughly a third of that in the L_X–λ relation, and that the L_X–λ scatter is intrinsic, i.e. will not be significantly reduced with larger sample sizes.

(iv) Our analysis of the scaling relation between L_X and T_X has shown that the fits are sensitive to the selection method of the sample, i.e. whether the sample is made up of clusters detected 'serendipitously' compared to those deliberately targeted by *XMM*. These differences are also seen in the L_X–λ relation and, to a lesser extent, in the T_X–λ relation. Exclusion of the emission from the cluster core does not make a significant impact to the findings. A combination of selection biases is a likely, but as yet unproven, reason for these differences.

(v) We have used our data to probe recent claims of anisotropy in the L_X–T_X relation across the sky (Migkas et al. 2020). We find no evidence of anistropy, but stress that this may be masked in our analysis by the incomplete declination coverage of the *SDSS* DR8 sample.

The methods outlined in this work have further been employed in the analysis of large cluster samples, such as those constructed from the RM analysis of the Dark Energy Survey data (Farahi et al. 2019; Zhang et al. 2019). Although optically selected samples are free from X-ray selection biases, when matching to available X-ray data, future archival studies should consider only the use of serendipitously detected X-ray clusters to avoid observer biases. Furthermore, future use of the *XMM* Cluster Survey data will be of critical importance
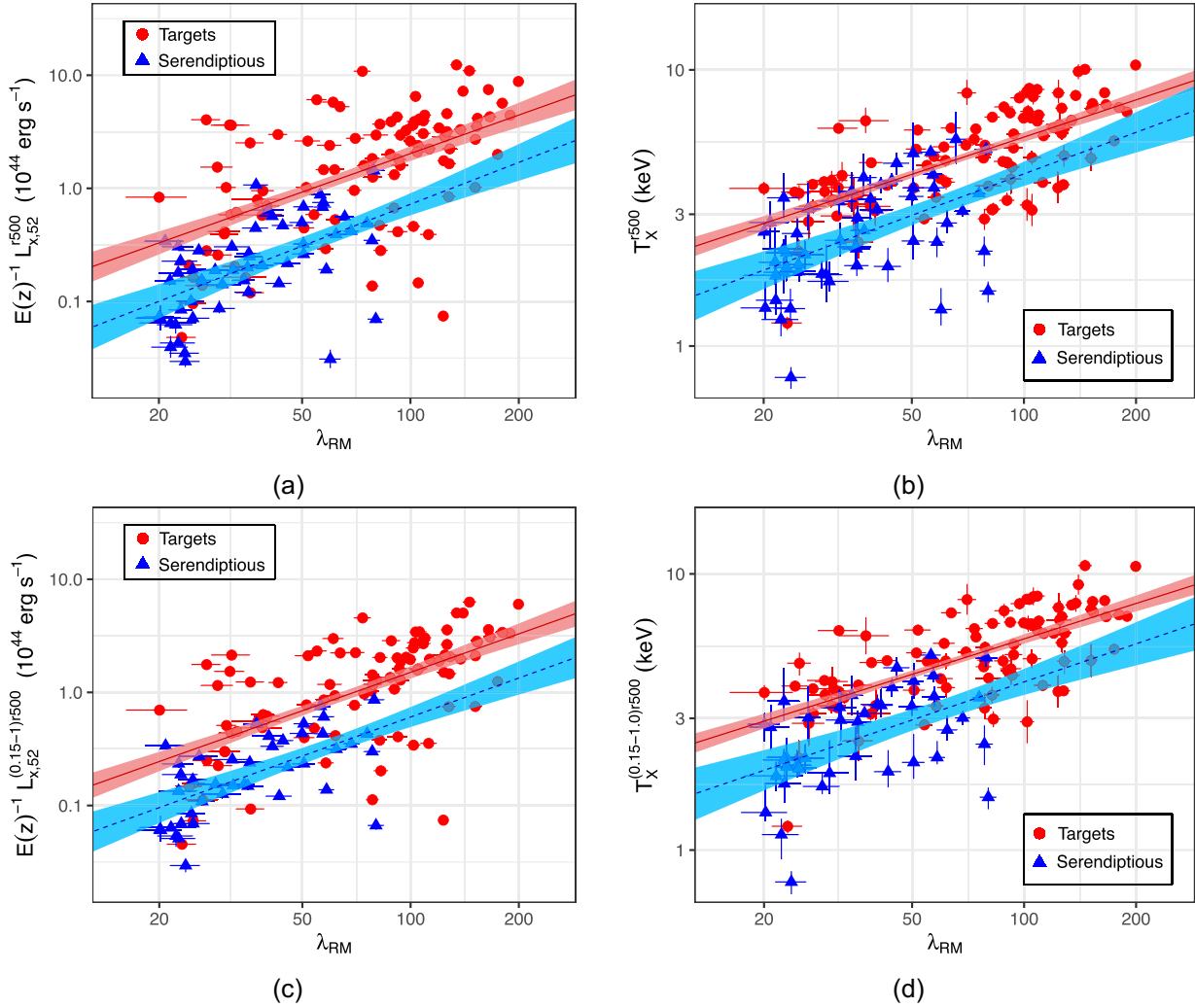
Figure 14. X-ray observable–richness relations of the SDSSRM–XCS$_{T_X, \text{vol}}$ sample, split between targeted (red circles) and serendipitous (blue triangles) clusters. Figure (a) plots the $L_{X,52}^{r500}$–λ_{RM} relation and (b) plots the T_X^{r500}–λ_{RM} relation, using the fiducial core included properties. Figure (c) plots the $L_{X,52}^{(0.15-1)r500}$–λ_{RM} relation and (d) plots the $T_X^{(0.15-1)r500}$–λ_{RM} relation, using core excluded properties. In each case, the red line and blue line represent a fit to the targeted and serendipitous clusters, respectively. Shaded regions around each fit highlights the 1σ uncertainty.
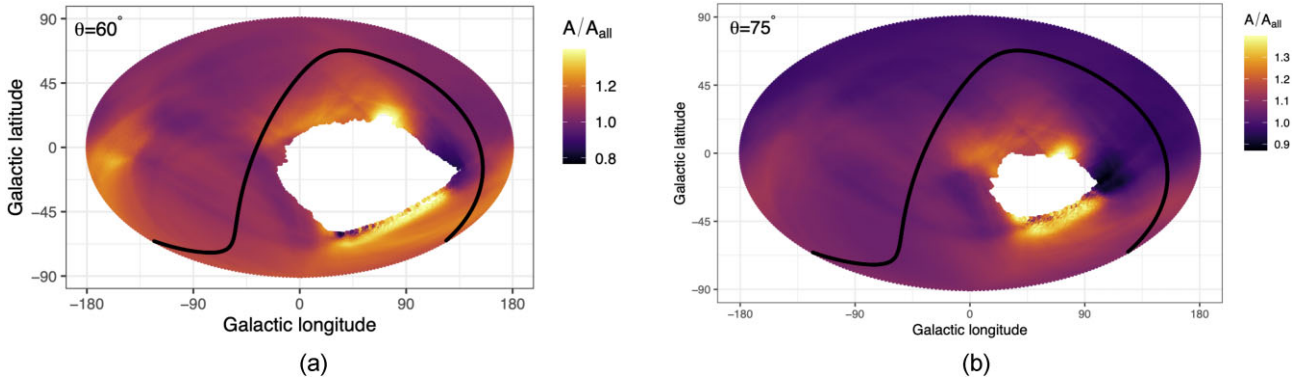
Figure 15. Ratio of the local best-fitting $L_{X,52}^{(0.15-1)r500}$–$T_X^{(0.15-1)r500}$ normalization (A) to the all sky normalization (A_{all}), as a function of sky position. Maps are created, assuming at each sky position, clusters within a cone of (a) $\theta = 60°$ and (b) $\theta = 75°$, are used for the local relation. The black line highlights the Galactic plane.

for upcoming cluster samples such as those constructed from the Legacy Survey of Space and Time undertaken by the Vera C. Rubin Observatory, of which currently $\approx$450 deg^2 of the LSST sky has been covered by *XMM*.

DATA AVAILABILITY

The data underlying this work can be found at:
http://users.sussex.ac.uk/pag22/SDSSRM-XCS/sdssrm-xcs-sample-data.csv, along with a table description:
http://users.sussex.ac.uk/pag22/SDSSRM-XCS/column_names.txt.

REFERENCES

Abbott T. M. C. et al., 2018, ApJS, 239, 18
Abbott T. M. C. et al., 2019, Phys. Rev. D, 100, 023541
Aguena M. et al., 2021, MNRAS, 502, 4435
Aihara H. et al., 2011, ApJS, 193, 29
Akritas M. G., Bershady M. A., 1996, ApJ, 470, 706
Arnaud K. A., 1996, in Jacoby G. H., Barnes J., eds, Proc. ASP Conf. Ser. Vol. 101, Astronomical Data Analysis Software and Systems V. Astron. Soc. Pac., San Francisco, p. 17
Arnaud M., Pointecouteau E., Pratt G. W., 2005, A&A, 441, 893
Cash W., 1979, ApJ, 228, 939
Cavagnolo K. W., Donahue M., Voit G. M., Sun M., 2009, ApJS, 182, 12
Clerc N., Pierre M., Pacaud F., Sadibekova T., 2012, MNRAS, 423, 3545
Clerc N. et al., 2014, MNRAS, 444, 2723
Dodelson S., Heitmann K., Hirata C., Honscheid K., Roodman A., Seljak U., Slosar A., Trodden M., 2016, preprint (arXiv:1604.07626)
Drlica-Wagner A. et al., 2018, ApJS, 235, 33
Farahi A., Evrard A. E., Rozo E., Rykoff E. S., Wechsler R. H., 2016, MNRAS, 460, 3900
Farahi A. et al., 2019, MNRAS, 490, 3341 (F19)
Freeman P. E., Kashyap V., Rosner R., Lamb D. Q., 2002, ApJS, 138, 185
Giles P. A. et al., 2016, A&A, 592, A3
Grandis S. et al., 2021, MNRAS, 504, 1253
HI4PI Collaboration, 2016, A&A, 594, A116
Hollowood D. L. et al., 2019, ApJS, 244, 22 (H19)
Horner D. J., 2001, PhD thesis, Univ. Maryland
Kelly B. C., 2007, ApJ, 665, 1489
Koulouridis E. et al., 2021, A&A, 652, A12
Kraft R. P., Burrows D. N., Nousek J. A., 1991, ApJ, 374, 344
Kravtsov A. V., Borgani S., 2012, ARA&A, 50, 353
Liu A. et al., 2022, A&A, 661, A2 (L22)
Lloyd-Davies E. J. et al., 2011, MNRAS, 418, 14 (LD11)
Lovisari L. et al., 2020, ApJ, 892, 102 (L20)
Mantz A., Allen S. W., Ebeling H., Rapetti D., Drlica-Wagner A., 2010, MNRAS, 406, 1773
Mantz A. B., Allen S. W., Morris R. G., von der Linden A., 2018, MNRAS, 473, 3072
Maughan B. J., Giles P. A., Randall S. W., Jones C., Forman W. R., 2012, MNRAS, 421, 1583
McClintock T. et al., 2019, MNRAS, 482, 1352
Mehrtens N. et al., 2012, MNRAS, 423, 1024
Migkas K., Schellenberger G., Reiprich T. H., Pacaud F., Ramos-Ceja M. E., Lovisari L., 2020, A&A, 636, A15 (Mig20)
Migkas K., Pacaud F., Schellenberger G., Erler J., Nguyen-Dang N. T., Reiprich T. H., Ramos-Ceja M. E., Lovisari L., 2021, A&A, 649, A151
Molham M. et al., 2020, MNRAS, 494, 161 (Mol20)
Oguri M., 2014, MNRAS, 444, 147
Oguri M. et al., 2018, PASJ, 70, S20
Piffaretti R., Arnaud M., Pratt G. W., Pointecouteau E., Melin J. B., 2011, A&A, 534, A109
Planck Collaboration VIII, 2011, A&A, 536, A8
Planck Collaboration XXIV, 2016, A&A, 594, A24
Pratt G. W., Croston J. H., Arnaud M., Böhringer H., 2009, A&A, 498, 361
Predehl P. et al., 2021, A&A, 647, A1
Romer A. K., Viana P. T. P., Liddle A. R., Mann R. G., 2001, ApJ, 547, 594
Rozo E., Rykoff E. S., 2014, ApJ, 783, 80 (RR14)
Rykoff E. S. et al., 2014, ApJ, 785, 104
Rykoff E. S. et al., 2016, ApJS, 224, 1
Sahlén M. et al., 2009, MNRAS, 397, 577
Schellenberger G., Reiprich T. H., Lovisari L., Nevalainen J., David L., 2015, A&A, 575, A30
Sereno M., 2016, MNRAS, 455, 2149
Sevilla-Noarbe I. et al., 2021, ApJS, 254, 24
Smith R. K., Brickhouse N. S., Liedahl D. A., Raymond J. C., 2001, ApJ, 556, L91
The LSST Dark Energy Science Collaboration, 2018, preprint (arXiv:1809.01669)
Turner D. J. et al., 2021, preprint (arXiv:2109.11807)
Wetzell V. et al., 2022, MNRAS, 514, 4696
Wilms J., Allen A., McCray R., 2000, ApJ, 542, 914
Wu H.-Y., Rozo E., Wechsler R. H., 2010, ApJ, 713, 1207
Zhang Y. et al., 2019, MNRAS, 487, 2578

## APPENDIX A: EXAMPLES OF PROBLEMATIC *XMM* OBSERVATIONS

Here, we show examples of SDSSRM clusters that were removed from the SDSSRM-*XMM* sample due to high levels of background, Fig. A1(a), and strong point source contamination, Fig. A1(b). See Section 2.3 for further details.
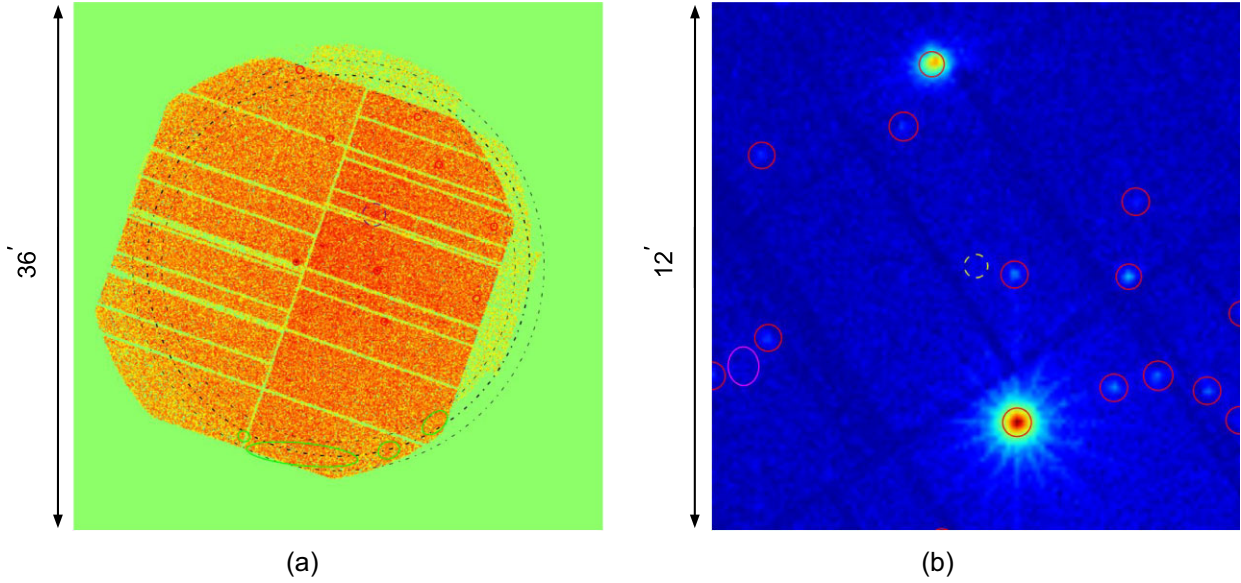
Figure A1. Examples of problematic *XMM* observations found during the visual inspection process described in Section 2.3. (a) Soft-band field-of-view image of the *XMM* observation ObsiD = 0556213801. The observation was rejected from further analysis because it is effected by periods of high background rates; (b) *XMM* image in the 0.5-2.0 keV band of the region surrounding SDSSRM cluster RMID = 42060 (centroid indicated with the dashed yellow circle). The cluster falls nearby to a bright point source that has created artefacts in the image (characterized by the 'spokes') and was subsequently dropped from the cluster sample.

## APPENDIX B: EXAMPLE OF A CLUSTER EXCLUDED FROM THE SDSSRM-XCS SAMPLE AFTER VISUAL INSPECTION

Here, we show an example of SDSSRM-XCS clusters that were initially matched to an extended XCS source, but after visual inspection (see Section 2.4), the X-ray emission was found not to be associated with the RM cluster. In Fig. B1, the SDSSRM-XCS cluster has been matched to an extended source where the X-ray emission comes from an outflow from a low redshift galaxy. The extended XCS source was deemed un-associated with the SDSSRM cluster in question.
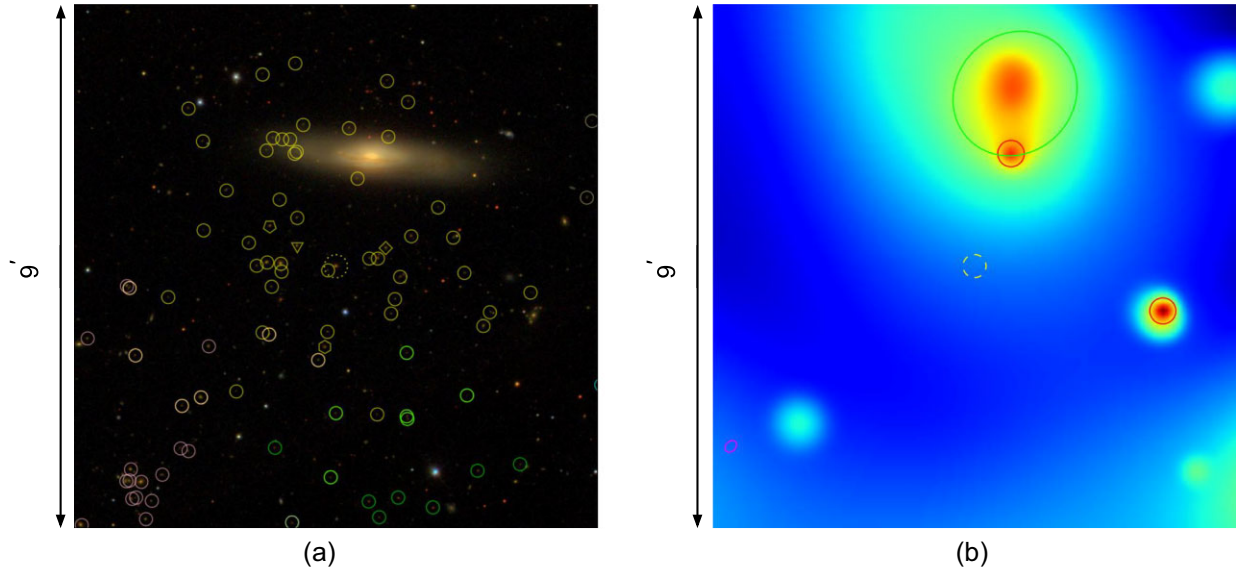
Figure B1. An example of SDSSRM cluster that is not physically associated with nearest extended X-ray source. (a) *SDSS* optical image of the cluster *SDSS* RMID = 55078, $z = 0.39$, and $\lambda = 26$. The yellow dashed circle shows the position of the RM defined central galaxy (remaining circles/shapes as defined in Fig. 2); (b) Corresponding *XMM* X-ray observation. Green (red) outlines highlight XAPA extended (point) sources. In this case, the extended emission is associated with an outflow from a nearby galaxy.

APPENDIX C: CLUSTERS EFFECTED BY MISPERCOLATION

In Section 2.4.1, we identified three pairs of clusters effected by mispercolation. In Fig. C1, an example of a mispercolated cluster is shown, and Table C1 highlights the three pairs of clusters effected by mispercolation and detail manual adjustments made to their properties.
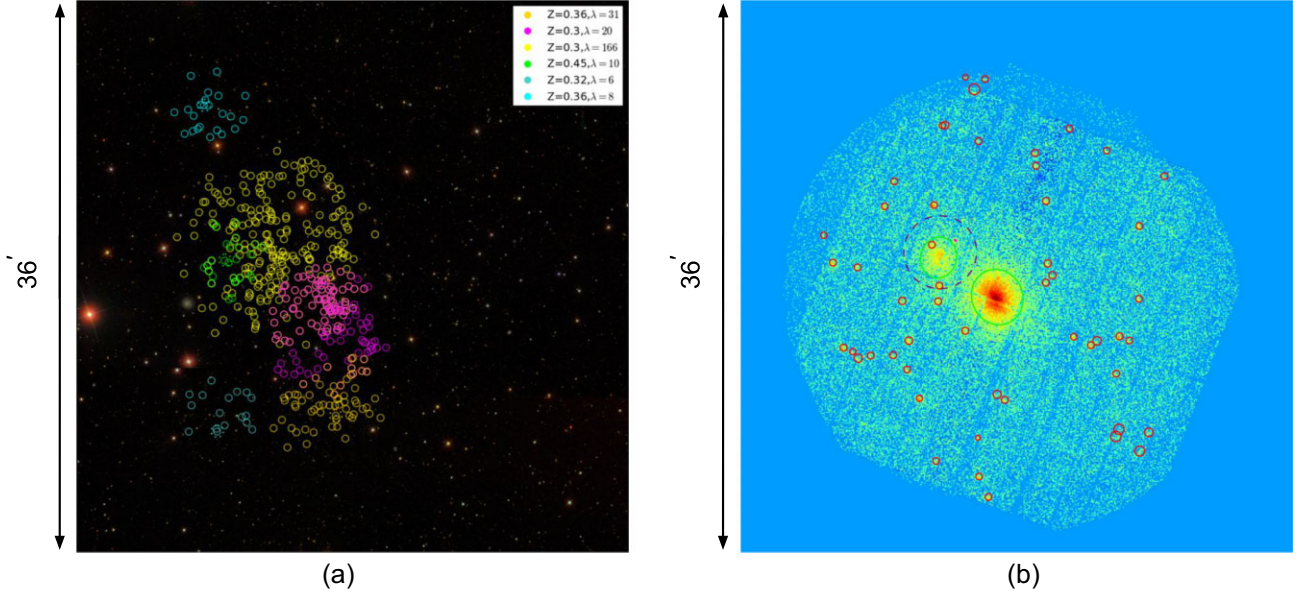
Figure C1. Example of a mispercolated cluster (as described in Section 2.4.1). Each image measures 36 armin × 36 arcmin on a side. (a) *SDSS* optical image with the yellow circles highlighting galaxies associated with the lower flux cluster ($\lambda_{RM} = 166$). Pink circles highlight galaxies RM associated with the higher flux cluster ($\lambda_{RM} = 20$). Other RM clusters nearby are highlighted by their respective colours (the colourbar inlay gives the redshift and richness of the highlighted clusters); (b) Corresponding *XMM* image.

Table C1. Clusters effected by mispercolation.

RMID	λ_{RM}	z	XCS match	Swap λ_{RM}	Notes
9	151	0.32	XMMXCS J100213.9+203222.7	15	Dropped from sample
12	15	0.32	XMMXCS J100227.5+203102.1	151	Retained, λ_{RM} swapped with RMID 9
21	39	0.30	XMMXCS J092021.2+303014.5	129	Retained, λ_{RM} swapped with RMID 23
23	129	0.29	XMMXCS J092052.5+302803.5	39	Retained, λ_{RM} swapped with RMID 21
34	166	0.30	XMMXCS J231148.8+034046.7	20	Retained, λ_{RM} swapped with RMID 41
41	20	0.30	XMMXCS J231132.6+033759.9	166	Retained, λ_{RM} swapped with RMID 34

APPENDIX D: ADDITIONAL SCALING RELATION FITS

In Table D1, we present results of our cluster scaling relation analyses using other apertures: core-excluded $(0.15–1)r_{500}$, and r_{2500}. The X-ray properties derived from these apertures are compared to those from our fiducial r_{500c} analysis in Fig. D1.
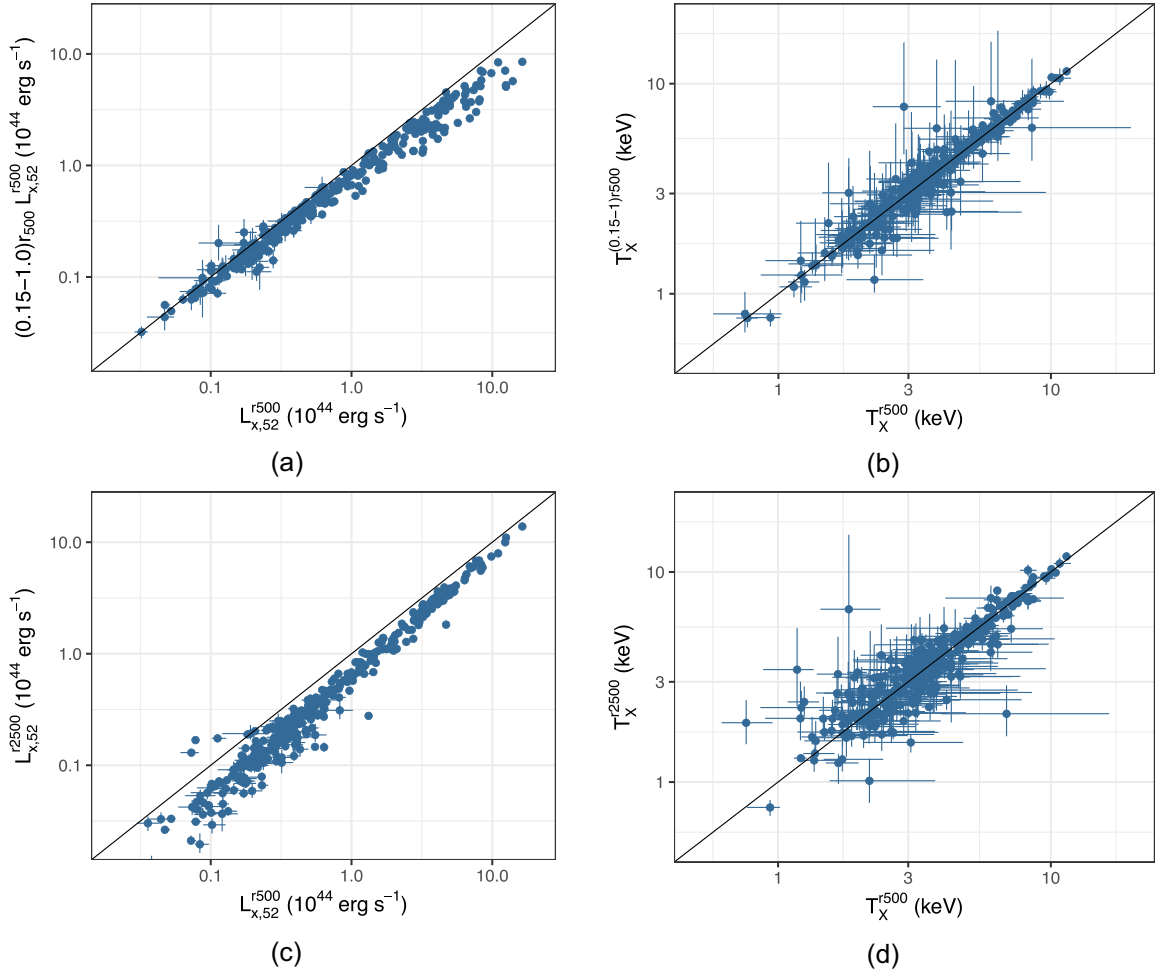
Figure D1. Comparison of cluster properties measured for our fiducial analysis (i.e. core-included, r_{500}). Plots (a) and (b) compare the core excluded (0.15–1.0r_{500}) luminosities and temperatures, respectively. Plots (c) and (d) compare r_{2500} luminosities and temperatures, respectively. In each plot, the 1:1 relation is highlighted by the solid black line.

Table D1. Best-fitting parameters of the scaling relations studied in this work when considering core excluded and r_{2500} cluster properties. In each case, parameters are given for the SDSSRM-XCS$_{T_X,\text{vol}}$ cluster sample, and the targeted and serendipitous sub-samples (as defined in Section 5.1). Best-fitting parameters are given for the L_X–T_X, T_X–λ_{RM}, and L_X–λ_{RM} relations, given by equations (3), (4), and (5), respectively (see Sections 4.1 and 4.2).

Relation (sample)	Normalization	Slope	Scatter	Figure
	Core-excluded relations			
$L_{X,52}^{(0.15-1)r500}$–$T_X^{(0.15-1)r500}$	A_{LT}	B_{LT}	σ_{LT}	
SDSSRM-XCS$_{T_X,\text{vol}}$	0.74 ± 0.03	2.46 ± 0.10	0.51 ± 0.04	–
Targets	0.73 ± 0.05	2.58 ± 0.16	0.53 ± 0.04	13(b)
Serendipitous	0.54 ± 0.07	1.84 ± 0.21	0.43 ± 0.06	13(b)
$L_{X,52}^{(0.15-1)r500}$–λ_{RM}	$A_{L\lambda}$	$B_{L\lambda}$	$\sigma_{L\lambda}$	
SDSSRM-XCS$_{T_X,\text{vol}}$	0.79 ± 0.06	1.49 ± 0.12	0.88 ± 0.06	–
Targets	1.06 ± 0.10	1.13 ± 0.16	0.88 ± 0.07	14(c)
Serendipitous	0.42 ± 0.07	1.15 ± 0.25	0.66 ± 0.08	14(c)
$T_X^{(0.15-1)r500}$–λ_{RM}	$A_{T\lambda}$	$B_{T\lambda}$	$\sigma_{T\lambda}$	
SDSSRM-XCS$_{T_X,\text{vol}}$	1.04 ± 0.03	0.58 ± 0.05	0.32 ± 0.02	–
Targets	1.17 ± 0.04	0.43 ± 0.05	0.26 ± 0.02	14(d)
Serendipitous	0.80 ± 0.07	0.46 ± 0.13	0.34 ± 0.04	14(d)

Table D1 – *continued*

Relation (sample)	Normalization	Slope	Scatter	Figure
		r_{2500} relations		
$L_{X,52}^{r2500}-T_X^{r2500}$	A_{LT}	B_{LT}	σ_{LT}	
SDSSRM-XCS$_{T_X,\mathrm{vol}}$	0.57 ± 0.04	2.89 ± 0.13	0.71 ± 0.05	–
Targets	0.68 ± 0.06	2.69 ± 0.19	0.71 ± 0.06	–
Serendipitous	0.44 ± 0.07	2.56 ± 0.33	0.62 ± 0.08	–
$L_{X,52}^{r2500}-\lambda_{\mathrm{RM}}$	$A_{L\lambda}$	$B_{L\lambda}$	$\sigma_{L\lambda}$	
SDSSRM-XCS$_{T_X,\mathrm{vol}}$	0.57 ± 0.06	1.69 ± 0.15	1.14 ± 0.07	–
Targets	0.88 ± 0.11	1.15 ± 0.20	1.13 ± 0.09	–
Serendipitous	0.43 ± 0.07	1.60 ± 0.24	0.66 ± 0.03	–
$T_X^{r2500}-\lambda_{\mathrm{RM}}$	$A_{T\lambda}$	$B_{T\lambda}$	$\sigma_{T\lambda}$	
SDSSRM-XCS$_{T_X,\mathrm{vol}}$	1.01 ± 0.03	0.59 ± 0.04	0.30 ± 0.02	12(d)
Targets	1.10 ± 0.04	0.49 ± 0.05	0.29 ± 0.02	–
Serendipitous	0.85 ± 0.06	0.42 ± 0.11	0.27 ± 0.04	–

APPENDIX E: REPLICATING THE OBSERVED L_X–T_X ANISOTROPY

In Section 5.2, we show the results of our investigation into the possible anisotropic behaviour of the L_X–T_X relation using the *SDSS*-XCS$_{T_X}$ cluster sample. While we conclude that the *SDSS*-XCS$_{T_X}$ sample does not have the required sky coverage to probe such effects, here, we show that the method (adopted from Mig20) indeed replicates the results shown in Mig20. Cluster data was obtained from Mig20 and using the replicated method (see Section 5.2), the results shown in Fig. E1.
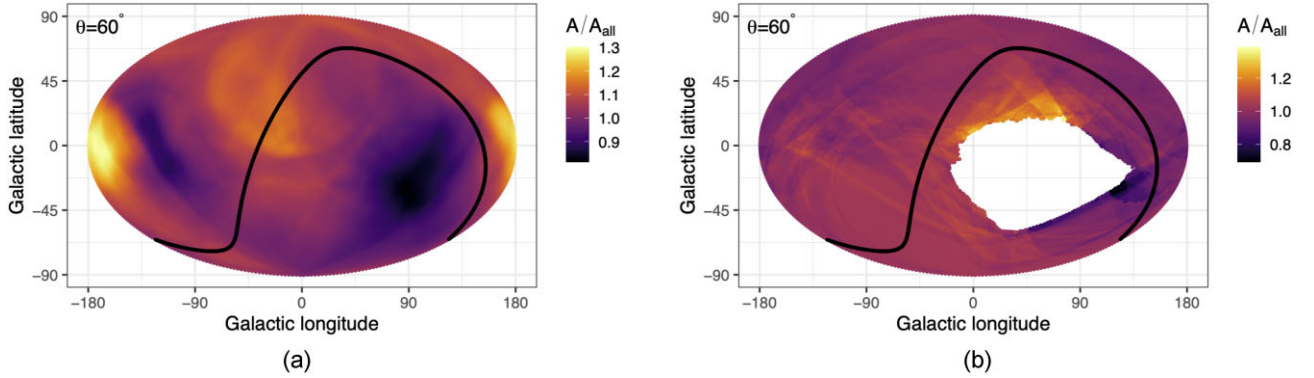
Figure E1. Ratio of the local best-fitting L_X–T_X normalization (A) to the all sky normalization (A_{all}), as a function of sky position. (a) The data used to create the map was taken from Mig20, hence replicating the results presented therein (see Mig20 fig 8). (b) The sky map was created using the SDSSRM–XCS$_{T_X}$ sample and following the updated method of Mig21, see Section 5.2. In each case, the maps are generated using cones of $\theta = 60°$ at each sky position and the black solid line represents the Galactic plane.

This paper has been typeset from a TEX/LATEX file prepared by the author.